

# Chapter 2

## Small-Angle X-Ray Scattering to Analyze the Morphological Properties of Nanoparticulated Systems



Oscar Moscoso Londoño, Pablo Tancredi, Patricia Rivas, Diego Muraca,  
Leandro M. Socolovsky, and Marcelo Knobel

### 2.1 Introduction

This chapter provides a global overview of the small-angle X-ray scattering (SAXS) theory and related concepts. The main goal of this document is to provide useful tools to analyze, fit, and simulate the SAXS data obtained from sets of different nanoparticulated systems. The emphasis will be placed on systems composed by single nanoparticles, as well as on those with a more complex morphology, standing out how the scattering intensity changes with nanoparticle size, with interparticle distance, or with nanoparticle morphology.

The structural nature of nanoscale materials can be studied by different techniques, including electron microscopy, X-ray diffraction, scattering, electron energy-loss spectroscopy, or neutron scattering, among others. All of these techniques are based on the scattering, absorption, or diffraction processes due to the interaction of an incoming radiation with matter. Basically, the structural information depends on the radiation source and its wavelength; for example,

---

O. Moscoso Londoño (✉)

Gleb Wataghin Institute of Physics, University of Campinas, Campinas, SP, Brazil

Faculty of Engineering, Autonomous University of Manizales, Manizales, Colombia

e-mail: [omoscoso@ifi.unicamp.br](mailto:omoscoso@ifi.unicamp.br); [oscar.moscosol@autonoma.edu.co](mailto:oscar.moscosol@autonoma.edu.co)

P. Tancredi · P. Rivas

Laboratory of Amorphous Solids, Faculty of Engineering, University of Buenos Aires, Buenos Aires, Argentina

D. Muraca · M. Knobel

Gleb Wataghin Institute of Physics, University of Campinas, Campinas, SP, Brazil

L. M. Socolovsky

Santa Cruz Regional Faculty, National Technological University – CIT-Santa Cruz (CONICET), Rio Gallegos, Argentina

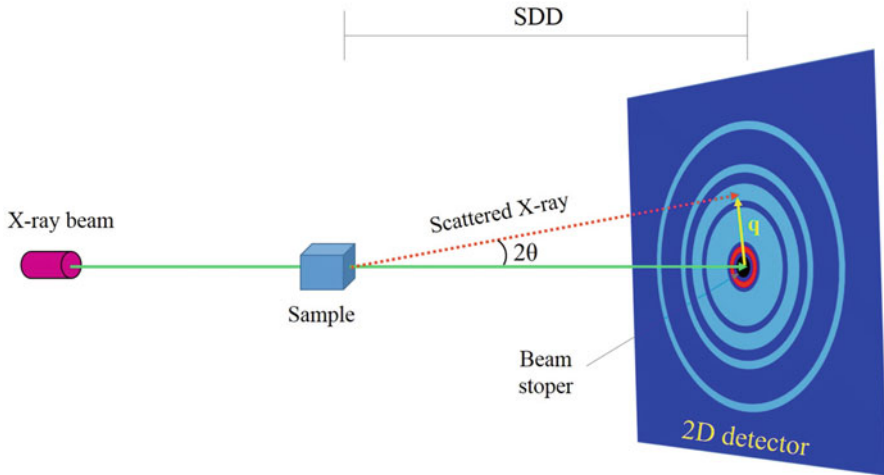
the use of radiation beams of X-rays, electrons, or neutrons, with wavelengths around 0.1 nm, permits the study of matter down to atomic resolution [1]. At these wavelengths it is possible to determine the crystal structure or the interplanar spacing of crystalline materials. By using neutron diffraction techniques, the atomic and magnetic structure of a material can also be studied. However, for a complete structural characterization, the study of the structure at the atomic level must be accompanied with morphological information. In this case, it is necessary to use X-ray or neutrons beams with wavelengths from 1 nm to thousands or even more [1]. Especially, for nanoscale systems composed by nanoparticles with size ranging between a few nanometers and  $\sim 100$  nm, the knowledge of the shape, the interparticle distance, the size nanoparticle distribution, the arrangement into a host matrix, as well as other information at superatomic scale are extremely relevant in order to obtain a complete picture of the structural features of the studied material. Fundamental morphological information can be accomplished by using the small-angle X-ray scattering (SAXS) technique. In nanoparticle research, a suitable data processing obtained from a SAXS measurement allows obtaining an overall picture of the nanoparticle sizes, shapes, and/or relative position of nanoparticles [2, 3]. In SAXS data treatment for a nanoparticulated system, it is generally assumed that each nanoparticle has a simple geometrical shape, such as sphere, ellipse, or rod, among others. Despite this simple geometric assumption, the SAXS technique has proven to be a powerful tool to determine the mean size of the nanoparticle, its size distribution, the shape, and the surface structure [3]; it is even possible to define the pair potential if the relative positions of the nanoparticles are known [4]. For other shapes, it is possible to compute a form factor that can be used in the SAXS equations.

The framework behind the SAXS technique is exploited in both scientific and industrial fields. These studies involve several branches, covering the metal alloys, polymers, biological macromolecules, emulsions, or porous materials, among others [2].

## **2.2 Small-Angle X-Ray Scattering**

### ***2.2.1 General Phenomenology***

Small-angle X-ray scattering (SAXS) is a technique where the elastic scattering of X-rays by a sample is recorded at very low angles (typically  $0.1\text{--}10^\circ$  measured from the beam axes). This angular range contains information regarding the structure of scatterer entities, like nanoparticles and micro- and macromolecules, among others. Depending of the studied systems, SAXS technique could provide information of the distances between partially ordered materials, pore sizes, as well as other data [5]. Besides, depending on the experimental setup, SAXS is capable of delivering structural information of objects whose size ranges between  $\sim 0.5$  and  $\sim 100$  nm.



**Fig. 2.1** Basic schematic SAXS setup

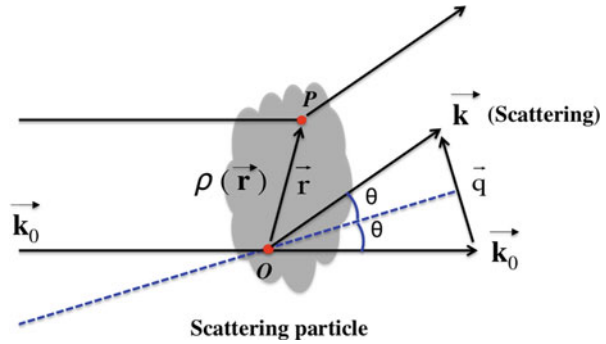
The limits depend on the photon energy, sample-to-detector distance (SDD), the pixel size and geometry of the X-ray detector, and size of the beam stopper (a SAXS setup is shown in Fig. 2.1) [6]. For example, larger objects, whose size is around  $\sim 1 \mu\text{m}$ , just produce perceptible scattering only at extremely small angles that means that the beam stopper size must be as small as possible; if not, the scattering waves hit the stopper and are not recorded by the detector [6].

To understand how the X-ray is scattered at low angles by a particle, it is necessary to know what happens when the X-rays irradiate a particle. In a very general way, it is possible to say that two phenomena occur: absorption and scattering. At the moment in which the X-rays hit the particle, one part of these will pass through the sample. Another part will be absorbed and transformed into heat and/or fluorescence radiation. The remaining fraction will be scattered into another direction of propagation [2]. The absorption processes occur with more probability at the absorption edges. At these edges, the electrons of the materials can be expelled leaving the atoms in an unstable state (with a hole). When the atom recovers its natural configuration, fluorescence radiation is emitted, with a given wavelength. The scattering processes can take place with or without energy loss, i.e., the scattered waves can have similar or different wavelength, compared to the incident radiation.

To analyze a scattering experiment, it is suitable to start assuming a fixed entity (or particle), with an arbitrary structure that can be represented by an electronic density function  $\rho(\vec{r})$ . Assuming that a monochromatic radiation beam, with  $\vec{k}_0$  as wave vector, hits this particle, the scattered wave direction will be defined by wave vector  $\vec{k}$ , as shown in Fig. 2.2.

Since scattering is assumed as an elastic process, the scattered wave has the same modulus of the incident wave, whose absolute value, in both cases, is given by  $2\pi/\lambda$ ,

**Fig. 2.2** Representation of the scattering process by a fixed particle



being  $\lambda$  the wavelength of the used radiation. This fact makes possible to establish the difference between the incident and scattered beams, which is given by:

$$\vec{q} = \vec{k} - \vec{k}_0, \quad (2.1)$$

where  $\vec{q}$  is the scattering vector. Rewriting the scattering vector can be defined as  $\vec{q} = 2\pi/\lambda (\vec{u} - \vec{u}_0)$ , being  $\vec{u}_0$  and  $\vec{u}$  the unitary vectors defining the incident and scatter beam directions, respectively. Since  $2\theta$  is the angle formed by the incident and scattered beams, then the magnitude of the scattering vector is:

$$q = 4\pi/\lambda \sin \theta \quad (2.2)$$

In a SAXS experiment, the scattering intensity  $I$  is measured as a function of  $q$ . It is well known that  $I(\vec{q})$  can be obtained by calculating the quadratic modulus of the amplitude function, defined in the reciprocal space ( $q$  space), of those waves scattered over the whole volume [6], i.e.,  $I(\vec{q}) = A(\vec{q}) \cdot A(\vec{q})^*/V = |A(\vec{q})|^2/V$ . The scattering amplitude  $A(\vec{q})$  is given by the Fourier transform of the electronic density,  $\rho(\vec{r})$ :

$$A(\vec{q}) = \int_V \rho(\vec{r}) \exp(-i\vec{q} \cdot \vec{r}) d\vec{r} \quad (2.3)$$

Consequently, applying the inverse Fourier transformation on Eq. 2.3, the electron density can be derived.

$$\rho(\vec{r}) = 1/(2\pi)^3 \int A(\vec{q}) \exp(i\vec{q} \cdot \vec{r}) d\vec{q} \quad (2.4)$$

Notice that  $-i\vec{q} \cdot \vec{r}$  is proportional to the phase shift  $\Delta\varphi = 2\pi\Delta S/\lambda = -(\vec{k} \cdot \vec{r} - \vec{k}_0 \cdot \vec{r})$ , being  $\Delta S$  the optical paths of two waves scattered by two volume elements, which in our case are represented by point  $O$  and  $P$  shown in Fig. 2.2. Using Eq. 2.1, the phase shift can be written as  $\Delta\varphi = -\vec{q} \cdot \vec{r}$ . Additional details of this procedure can be found in a recent chapter [6].

Once  $A(\vec{q})$  is determined, the dispersion intensity can be written as:

$$I(\vec{q}) = \int_V^0 a \int_V^0 \rho(\vec{r}') \rho(\vec{r}' - \vec{r}) \exp(-i\vec{q} \cdot \vec{r}) dr dr' \quad (2.5)$$

Here, it is possible to introduce the so-called correlation function,  $\gamma(\vec{r})$  [7], which is particularly important in non-particulated systems, such as microemulsions or metal alloys, since it describes the variation of density as a function of the distance measured from a reference point. This function is defined as:

$$\gamma(\vec{r}) = \frac{1}{V} \int_V^0 \rho(\vec{r}') \rho(\vec{r}' - \vec{r}) dr = \frac{1}{V} P(r), \quad (2.6)$$

where  $P(r)$  is a similar function to those obtained from crystallographic methods, which is called the Patterson function. Crystallographically speaking it is basically a map of all atom-to-atom vectors in a crystal, which can be expressed as.  $P(u, v, w) = \int \rho(x, y, z) \rho(x + u, y + v, z + w) dx dy dz$ , being  $\vec{u}$ ,  $\vec{v}$ , and  $\vec{w}$  the vectors formed between positions  $x$  and  $x + u$ ,  $y$  and  $y + v$ , and  $z$  and  $z + w$ , respectively. This function contains information regarding all vectors between every two atoms of all the molecules within the crystal [8]. In a scattering experiment of a macromolecule, for example, the  $P(r)$  function takes the name of pair-density distribution function or simply pair-distribution function. In this case,  $P(r)$  provides information of the electron distances of the scattering entities; in others words, it is the probability of finding another scatterer entity at a position  $\vec{r}$  with respect to the one placed at the origin [9]. The main difference between the Patterson function and the pair-distribution function lies on that  $P(r)$  provides a radial average and does not give rise to vectors between scattering entities. In that sense,  $P(r)$  can be determined if the electronic density  $\rho(\vec{r})$  is known. Therefore,  $P(r) = r^2 \left\langle \int_V^0 \Delta\rho(\vec{r}) \Delta\rho(\vec{r} + \vec{r}') d\vec{r}' \right\rangle$  [8]. The brackets  $\langle \rangle$  represent an average over

the analyzed sample volume  $V$ , and  $\Delta\rho(\vec{r})$  is the average electron density, which can be defined as  $\Delta\rho(\vec{r}) = \rho(\vec{r}) - \rho_S$ . Here,  $\rho(\vec{r})$  is the electron density of the molecules of interest, and  $\rho_S$  is assumed to be constant that represents the electron density of the host medium, which can be, for example, pure water ( $\sim 0.33 \text{ e}^- \text{ \AA}^{-3}$ ).

Then, using Eqs. 2.5 and 2.6, the scattering intensity can be rewritten as:

$$I(\vec{q}) = \int_V^0 \gamma(\vec{r}) \exp(-i\vec{q} \cdot \vec{r}) dr = \frac{1}{V} \int_V^0 P(\vec{r}) \exp(-i\vec{q} \cdot \vec{r}) dr \quad (2.7)$$

As can be noted,  $\gamma(\vec{r})$  can be indirectly determined by the inverse Fourier transformation of the experimental scattering function:

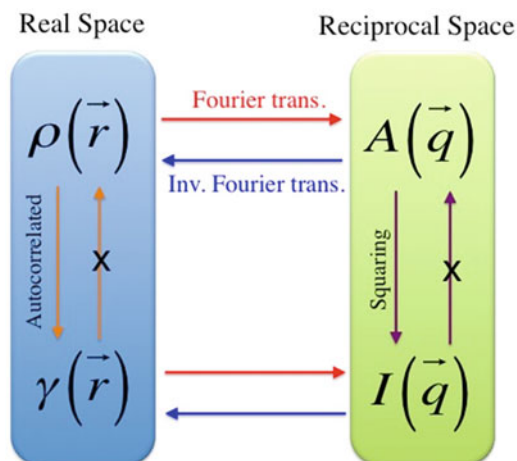
$$\gamma(\vec{r}) = \frac{1}{(2\pi)^3 V} \int I(\vec{q}) \exp(i\vec{q} \cdot \vec{r}) d\vec{q} \quad (2.8)$$

This procedure is regularly used in order to avoid problems of the discrete sampling of the scattering intensity curve over a finite range [10].

In this first section, the main concepts related to the scattering processes from non-particulated entities have been introduced. Some of them are defined in the real space, such as electron density  $\rho(\vec{r})$ , which is directly linked to the correlation function  $\gamma(\vec{r})$ , as well as with the pair-distribution function  $P(r)$ . While, in the reciprocal space, the scattering amplitude  $A(\vec{q})$  and the scattering intensity  $I(\vec{q})$  were defined. Some of these parameters can be connected mathematically by the Fourier transformations. For example, the electron density  $\rho(\vec{r})$  with the scattering amplitude  $A(\vec{q})$  as well as the autocorrelation function  $\gamma(\vec{r})$  with the scattering intensity  $I(\vec{q})$  (see Fig. 2.3). However, there are a series of facts/restrictions, whether mathematical or instrumental, that must be taken into account in order to correctly determine and connect the mentioned quantities, for instance, the function  $\gamma(\vec{r})$  can be determined from  $\rho(\vec{r})$  (Eq. 2.5), but inversely  $\rho(\vec{r})$  cannot be calculated [6]. Similarly situation happens with  $A(\vec{q})$  and  $I(\vec{q})$ , where the scattering intensity can be determined by squaring the scattering amplitude, but not in the opposite direction, as shown in Fig. 2.3. On the other hand, the mathematical properties of the Fourier transformations allow to connect the expressions of the real space with the reciprocal ones, as mentioned above. Here, the challenge lies on choosing the suitable reciprocal resolution for the desired scattering experiment. For instance, it is well known that in a scattering experiment at low angles (SAXS), the scattering amplitude  $A(\vec{q})$  is obtained for a small volume in the  $q$  space [6], and hence, the structural features that can be extracted from  $\rho(\vec{r})$  will be restricted to those at *low resolution*.<sup>1</sup> On the other hand, if  $A(\vec{q})$  is determined for a large volume in the  $q$  space and the structure of the studied material is sufficiently ordered, then it is possible to obtain an expression for the electron density, containing structural information of *high resolution*.<sup>1</sup>

<sup>1</sup>Notice that *high* or *low resolution* refers to those structural properties at atomic or superatomic level, respectively.

**Fig. 2.3** Pathways between the main expressions derived from a scattering framework. (Graph adapted from Amemiya and Shinohara [11])



In a SAXS experiment, a one- or two-dimensional (1-D or 2-D) detector collects the experimental information by counting the scattered photons as a function of the distance to the beam axes, measured as an angular position to subsequently form a 1-D or 2-D scattering pattern. It can be expressed as a function of the scattering vector  $q$ , or by using Eq. 2.2, it is also possible to express the position of each pixel in terms of the scattering angle ( $2\theta$ ). In isotropic systems, a 2-D graph can be azimuthally averaged to give a one-dimensional scattering curve. Especially, for colloidal systems containing randomly oriented nanoparticles, the majority of the obtained 2-D patterns have isotropic scattering features, which can be azimuthally averaged [3]. Anisotropic systems, such as lamellar structures or ordered polymers [12], among others, cannot be azimuthally averaged because the 2-D pattern is not isotropic along the azimuthal direction [3]. On these cases, the scattering profiles can be represented using other coordination systems.

As can be noticed, the scattering intensity  $I(\vec{q})$  is obtained instead of the scattering amplitude<sup>2</sup>  $A(\vec{q})$ . This condition implies that Eq. 2.4 cannot be applied in order to determine the electron density function, which, in fact, contains the structural information. To obtain accurate *low-resolution* structural features of nanosystems, including nanoparticles, nanowires, and nanopillars, among others, this obstacle is often overcome by proposing a model that includes shapes, sizes and its distributions, distances between nanoparticles, as well as other features at superatomic level, whose initial conditions can be refined by means of a SAS software package. Depending on the studied systems or if the scattering entities are interacting, it will be necessary to introduce a function to correlate them.

<sup>2</sup>Experimentally it is not possible to obtain the amplitude and phase of the scattering amplitude  $A(\vec{q})$ . Experimental SAXS data allows determining the modulus of  $A(\vec{q})$ , but the phase remains unknown.

This procedure requires a previous knowledge of the system. Some of these features can be initially determined using other techniques, as, for example, X-ray diffraction (XRD) and scanning or transmission electron microscopy (SEM/TEM).

### 2.2.2 *Small-Angle X-Ray Scattering from Isotropic and Non-fixed Nano-objects*

Considering a centrosymmetric, randomly oriented and non-fixed particle and assuming a constant electron density within the particle ( $\gamma(\vec{r}) = \gamma(r)$ ) and null outside it, then the obtained scattering intensity will be isotropic, and it will contain the scattering information of all possible orientations. Under these assumptions, the factor  $\exp(-i\vec{q} \cdot \vec{r})$  can be averaged as  $\langle \exp(-i\vec{q} \cdot \vec{r}) \rangle = \frac{\sin(qr)}{qr}$  [1, 6]. Thus, the scattering intensity for this particle (Eq. 2.7) becomes:

$$I_p(\vec{q}) = 4\pi V \int_0^\infty \gamma(r) \frac{\sin qr}{qr} r^2 dr, \quad (2.9)$$

being  $V$  the particle volume. From this result, it is possible to infer that for a set of identical and uncorrelated particles, the total scattering intensity can be expressed as:

$$I(q) = NI_p(q) \quad (2.10)$$

where  $N$  is the number of particles per unit volume and  $I_p(q)$  is the scattering intensity produced by a single particle. Notice that the solution of Eq. 2.10 depends on the  $q$  range. For example, when solving this equation at low- $q$  range, the so-called Guinier law is obtained, sometimes expressed as Guinier approximation [13]. While at high- $q$  values, the solution takes the name of Porod law [14].

#### 2.2.2.1 **Low- $q$ Regime: Guinier Law**

According to the Guinier approximation, the scattering intensity at low- $q$  depends on the radius of gyration of the particle. To develop the solution for Eq. 2.10 at small- $q$  values, it is necessary to look back to Eq. 2.3, which describes the scattering amplitude in terms of the electron density function. Thus, expanding the exponential factor of this equation, it becomes:

$$A(q) = \int \rho(r) dV - i \int qr \rho(r) dV - \frac{1}{2!} \int (qr)^2 \rho(r) dV \dots \quad (2.11)$$



Assuming an isotropic system ( $\rho(r) = \rho_0$ ) with  $r$  taken from the center of the mass, then the first integral becomes  $\rho_0 V$ , and the second one will be null. Therefore, Eq. 2.11 can be rewritten as  $A(q) = \rho_0 V - \frac{1}{2}(qr)^2 \int \rho(r) dV \dots$  or also:

$$A(q) = \rho_0 V \left[ 1 - \frac{1}{2}(qr)^2 \dots \right] \quad (2.12)$$

Remembering that the scattering intensity can be obtained by squaring  $A(q)$ , then:

$$I(q) = (\rho_0 V)^2 \left[ 1 - (qr)^2 + \frac{1}{2}(qr)^4 \dots \right] \quad (2.13)$$

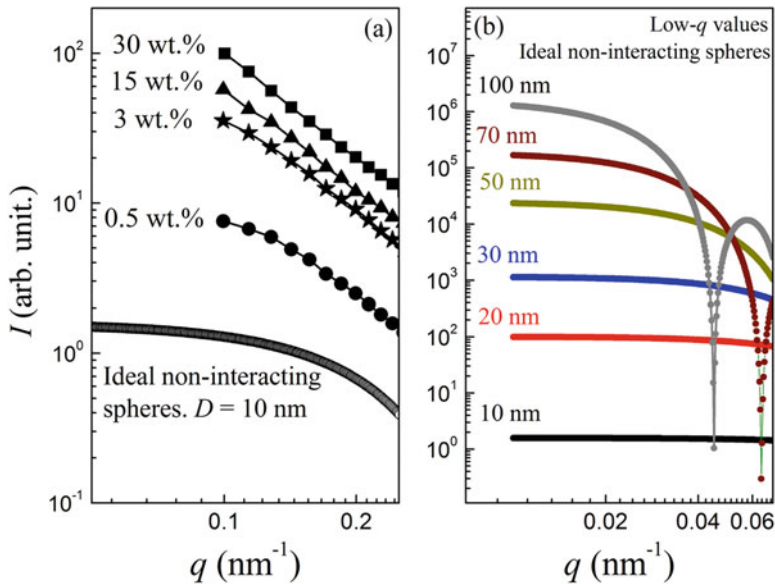
At low- $q$  values, it is clear that  $(qr)^2 \gg (qr)^4$ , whereby the scattering intensity at low- $q$  turns into:

$$I(q \rightarrow 0) \cong (\rho_0 V)^2 \left[ 1 - (qr)^2 \dots \right] \quad (2.14)$$

A simple way to relate  $r$  with the radius of gyration  $R_g$  is bearing in mind that vector  $r$  written in the Cartesian coordinate system is  $r = \vec{x}^2 + \vec{y}^2 + \vec{z}^2 + 2\vec{x}\vec{y} + 2\vec{x}\vec{z} + 2\vec{y}\vec{z}$  and then  $(qr)^2 = q_x^2 \vec{x}^2 + q_y^2 \vec{y}^2 + q_z^2 \vec{z}^2 + 2q_x^2 q_y^2 \vec{x}\vec{y} + 2q_x^2 q_z^2 \vec{x}\vec{z} + 2q_y^2 q_z^2 \vec{y}\vec{z}$ . As the system was assumed to be isotropic, then  $\vec{x}\vec{y} = \vec{x}\vec{z} = \vec{y}\vec{z} = 0$  and  $\vec{x}^2 + \vec{y}^2 + \vec{z}^2 = \frac{1}{3}R_g^2$  [15]. With this tools at hand, the scattering intensity acquires the form of  $I(q \rightarrow 0) \cong (\rho_0 V)^2 \left[ 1 - q^2 \frac{1}{3}R_g^2 \dots \right]$  or well, reduced to an exponential form,  $I(q \rightarrow 0)$ :

$$I(q \rightarrow 0) \cong (\rho_0 V)^2 \exp\left(-q^2 \frac{1}{3}R_g^2\right) \quad (2.15)$$

The latter equation is known as the Guinier law, which for ideal particle systems provides the most simple and accurate method to determine the size of a particle using SAXS [3]. Notice that this equation can be applied on experimental data to obtain the radius of gyration of the scattered objects. Basically, the procedure consists in plotting the  $\log[I(q)]$  against  $q^2$  for the data obtained at low- $q$  values and whose trend is more or less linear. However, when determining  $R_g$  from the Guinier plot, the accuracy of  $R_g$  is limited by the minimum  $q$  value, which in fact is determined by the minimum scattering angle at which the scattering radiation is detected [1]. The nonlinearity of  $I(q)$  against  $q^2$  at low- $q$  can be mainly attributed to two factors, the measured  $q$  range and possible interference effects of those



**Fig. 2.4** (a) Comparison between four experimental SAXS curves at low- $q$  for a set of 10 nm nanoparticles loaded in four different concentrations in a non-conductive polymer matrix and the simulated SAXS curve for a set of noninteracting and monodisperse 10 nm nanoparticles. (b) Simulated SAXS curves for ideal systems composed for spherical nanoparticles with different diameters

waves scattered by neighboring particles. The first case commonly occurs on particle systems whose size ranges around 100 nm; for these kinds of objects, it is necessary to record the experimental scattering intensities at extremely low- $q$  values. On the other hand, if the studied system is composed of densely packed particles, such as concentrated nanoparticle solution or percolated samples, the relative distances between the scattering particles will be in the same order of the particle size, or it could even be smaller. On these materials, interference effects between the scattered waves take place, producing deviations of the Guinier trend. To model these interference effects, a structure factor  $S(q)$  must be added to the scattering intensity, whose framework will be discussed in the next sections.

Figure 2.4 presents the experimental and simulated SAXS curves at low- $q$  representing the effects of size and agglomeration on the Guinier law. From Fig. 2.4a it is possible to appreciate the effects of the nanoparticle concentration on the SAXS pattern linearity at low- $q$ . Here, four experimental SAXS curves are shown, which correspond to systems composed of nanoparticles of mean size  $\sim 10$  nm, loaded in a polymer matrix with concentrations of 0.5 wt%, 3 wt%, 15 wt%, and 30 wt%. As can be noticed, the increase in the nanoparticle concentration generates a greater deviation from the Guinier behavior. For comparison purposes it is also presented the simulated SAXS curve for a system composed by noninteracting and monodisperse spherical nanoparticles of 10 nm of diameter, where the linearity of

**Table 2.1** Radius of gyration for particles of known geometry

Sphere of radius $R$	$R_g^2 = \frac{3}{5} R^2$	[1]
Thin rod with length $L$	$R_g^2 = \frac{L^2}{12}$	[15]
Thin circular disk with radius $R$	$R_g^2 = \frac{R^2}{2}$	[15]
Spherical shell with inner radius $R_A$ and outer radius $R_B$	$R_g^2 = \frac{3}{5} \frac{R_B^5 - R_A^5}{R_B^3 - R_A^3}$	[1]
Ellipse with semiaxes $a$ and $b$	$R_g^2 = \frac{a^2 + b^2}{4}$	[1]
Ellipsoid with semiaxes $a$ , $b$ , and $c$	$R_g^2 = \frac{a^2 + b^2 + c^2}{5}$	[1]
Circular cylinder with radius $R$ and height $L$	$R_g^2 = \frac{L^2}{12} + \frac{R^2}{2}$	[16]
Hollow circular cylinder with inner radius $R_A$ , outer radius $R_B$ , and height $L$	$R_g^2 = \frac{R_A^2 + R_B^2}{2} + \frac{L^2}{12}$	[1]
Elliptical cylinder with semiaxes $a$ and $b$ and height $L$	$R_g^2 = \frac{a^2 + b^2}{4} + \frac{L^2}{12}$	[1]
Squared platelets with thickness $T$ and length $L$	$R_g^2 = \frac{L^2}{6} + \frac{T^2}{12}$	[16]
Gaussian chain of $N+1$ segments connected by $N$ bonds of fixed length $l$	$R_g^2 = \frac{Nl^2}{6}$	[15]

the SAXS pattern is clearly observed at low- $q$ . In Fig. 2.4b, the scenario is different; here six simulated SAXS curves for ideal spheres with diameters ranging between 10 and 150 nm are presented. Each curve represents the SAXS intensity behavior at the Guinier zone; from these curves it is clear that the Guinier trend is lost at lower- $q$  values as the size of the scattering objects is greater; hence the Guinier approximation is only valid for the interval  $q_{\text{MIN}}$  to  $q$  in which the linear dependence is followed [1]. Summarizing, it must be noticed that for a correct estimation of the radius of gyration, it is necessary to take into account effects like the aggregation. Also it is crucial to propose a precise ratio between the measuring  $q$  range and the particle size.

Assuming the most typical case, in which the scattering objects are considered solid spheres, the radius of gyration can be directly estimated by determining  $R_g$  from the slope of the  $\log[I(q)]$  vs.  $q^2$  plot, which is equal to  $R_g^2/3$ . For non-spherical particles but of known geometric like cylinders, ellipses, or platelets, for example, the employment of a generalized Guinier plot, it is also useful to determine the radius of gyration of these objects [5]. Some expressions to derive the radius of gyration through the geometric dimensions of their bodies are listed in Table 2.1.

The previous expressions were developed for highly ideal systems, i.e., they neglect features existing in any real sample, such as particle size distribution effects. In order to consider the distributed properties found in almost all of the real samples, it is necessary to consider the individual contribution of each scattering object. If the studied sample is composed of particles with a narrow size distribution, the distributed properties can be taken into account by considering the averaged parameters at the Guinier law (Eq. 2.15). Then, the Guinier law becomes  $I(q \rightarrow 0) \cong \rho_0^2 \langle V^2 \rangle \exp\left(-q^2 \frac{1}{3} \langle R_g^2 \rangle\right)$ , where  $\langle V \rangle$  is the volume average of all

scattered particles contained in the sample and  $\langle R_g \rangle$  is the so-called Guinier average approach (weighted average [6]), which is defined as:

$$\langle R_g \rangle^2 = \frac{\int (V R_g)^2 dR_g}{\int V^2 dR_g}, \quad (2.16)$$

Solving Eq. 2.16 for a set of spherical uncorrelated nanoparticles with a narrow size distribution, the radius of gyration can be determined by  $\langle R_g \rangle^2 = \langle R^8 \rangle / \langle R^6 \rangle$ . It is extremely important to keep in mind that the above expression comes from averaging operations, where the statistical weight of those larger particles will be greater in comparison to the small ones. In that sense, if the studied sample is highly polydisperse or if this is composed by several sets of particles, each one with different mean size, then the estimation of the radius of gyration will be biased toward  $R_g$  values linked with larger scattering particles. This effect is commonly attended by proposing different sets of scattering contributions as necessary. For example, if we have a sample composed of  $n_i$  sets of particles, each one with mean size  $\langle D \rangle_i$ , then, the total scattering intensity can be expressed as the sum of all contributions; therefore  $I(q) = N_1 I_1(q) + N_2 I_2(q) + \dots$ , being  $N_i$  the number of particles belonging to each family.

### 2.2.2.2 High- $q$ Regime: Porod Law

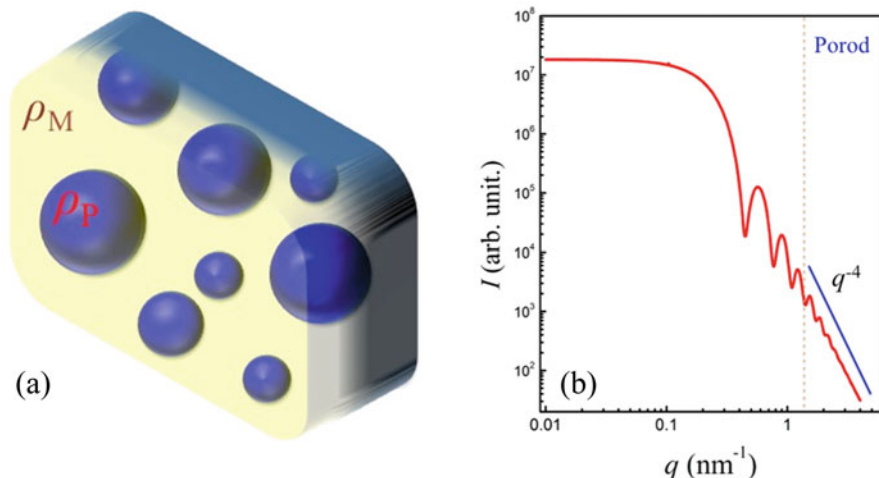
The Porod law describes the behavior of the scattering intensity at the high- $q$  region. As mentioned in the previous section, the scattering intensity ( $I(q)$ ) and the correlation function ( $\gamma(\vec{r})$ ) are mathematically connected by the Fourier transform properties. Analyzing the properties of these functions, one can establish that for high- $q$  values ( $q \rightarrow \infty$ ), the smallest values of  $r$  have prevalence in  $\gamma(\vec{r})$ . Mathematically speaking, it means that for small  $r$ , the correlation function can be expanded in Taylor series [13], obtaining the following equivalence:

$$\gamma(r) = \gamma(0) \left[ 1 + \frac{1}{4} \frac{S}{V} r + \dots \right] \quad (2.17)$$

being  $S$  the specific surface of the scattering particle in the illuminated sample volume  $V'$  or well  $S/V'$  can be interpreted as the illuminated area per unit volume. Replacing the expanded expression for the correlation function ( $\gamma(\vec{r})$ ) in Eq. 2.9 and solving the integral for  $q \rightarrow \infty$ , the scattering intensity expression becomes:

$$I(q \rightarrow \infty) = \frac{2\pi\rho^2 S}{q^4} \quad (2.18)$$

Then, it can be noticed that Eq. 2.18, named the Porod law, indicates the asymptotic behavior of  $I(q)$  when the scattering vector  $q$  tends to be large values. As an important point to highlight, the dependence of  $I(q \rightarrow \infty)$  with  $S$  can be harnessed to examine the surface of those particles illuminated in a SAXS experiment. As



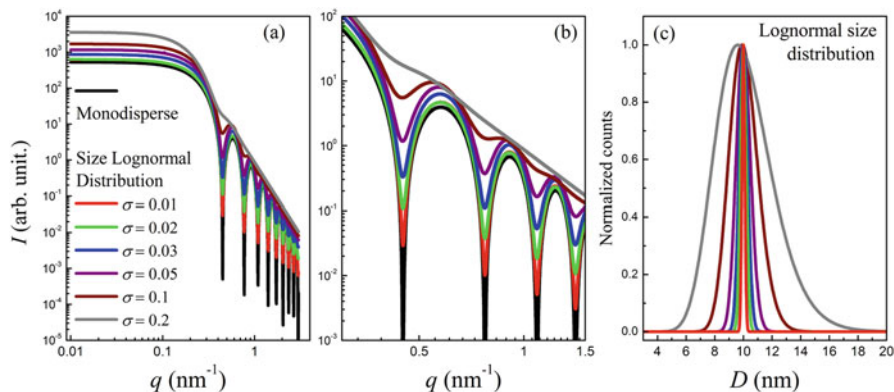
**Fig. 2.5** (a) Schematic representation of a set of polydisperse and uncorrelated particles loaded in a matrix with a constant electron density. (b) SAXS-simulated spectra for a set of polydisperse particles with 10 nm as the mean size. Here, a lognormal size distribution was proposed ( $\sigma = 0.05$ )

in any real sample, the scattering particles are surrounded by a specific medium (as is shown in Fig. 2.5), with a different electronic density; due to this fact, it is convenient to express the Porod law taking into account both electron densities. Then, assuming that both the electron densities of the particles and surrounding media are isotropic, the Porod law is rewritten as  $I(q \rightarrow \infty) = 2\pi(\rho_P - \rho_M)^2 S/q^4$ , being  $\rho_P$  and  $\rho_M$  the constant electronic densities of the scattering particles and the surrounding medium, respectively. Additional details of this procedure are found in a recent chapter book [6].

The Porod law can also be applied for systems composed of nanobodies with other simpler geometric shapes, for example, cylinders or planar objects. Independently of the shape of the scattering particles, the Porod law is applicable if a sharp interface between the particle and the medium is present.

### 2.2.2.3 Intermediate- $q$ Regime: The Role of the Polydispersity

The supposition that a sample is constituted by a set of identical particles is rarely real. In most real samples, naturally occurring or lab synthesized, there is a combination of particles with different sizes and shapes. In these cases, SAXS is a powerful technique from which information as regards the shape and/or the size distribution can be obtained [17, 18]. We are going to start proposing a sample composed by  $N$  particles of the same shape and isotropic electronic density but whose sizes oscillates moderately around a mean value, to then analyze the main alterations on a set of SAXS patterns produced by ensembles of spherical particles with different polydispersities. Despite in this section, we focus the discussion on



**Fig. 2.6** (a) Simulated SAXS curves for spherical particles varying the degree of polydispersity. These simulations were carried out proposing a size distribution that follows a lognormal function. (b) Representative zoom of the intermediate- $q$  region. (c) Simulated lognormal-type size distributions

particles with the simplest shape (spheres); one of the main challenges derived from a SAXS study is to determine the particle shape, an issue that can be overcome employing shape-independent modeling methods [19, 20].

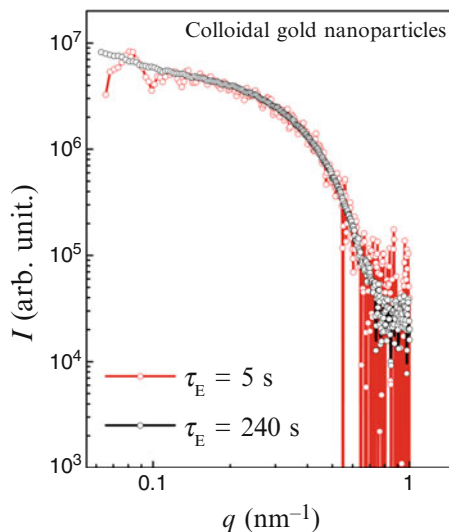
Figure 2.6 shows seven simulated SAXS curves; these curves were constructed assuming a scattering entity of known shape, spheres in this case (form factors will be introduced in next section). Each scattering intensity curve is related to a set of particles with mean diameter of 10 nm whose size distribution follows a lognormal-type size distribution  $f(d)$ , except for that curve representing a monodisperse system (black curve). As can be noted in Fig. 2.6a, b, the curve silhouette is extremely sensitive to the polydispersity degree (controlled via the lognormal standard deviation  $\sigma$ ), especially on the oscillatory behavior of the curve at intermediate- $q$  values. Here one can also note that for monodisperse samples, as well as for those samples with low polydispersity ( $\sigma < 0.05$ ), the oscillatory behavior is perfectly perceived at intermediate- $q$  values.

Despite that in this example a lognormal function was adopted to represent the particle polydispersity, there are other functions which depend on the polydispersity nature of the studied sample and can represent this feature very well. Some of these are the Schultz-Zimm and the Gaussian distributions, among many others. A few expressions often used to represent the polydispersity in samples composed by nanoparticles are listed in Table. 2.2.

As discussed for previous regions (Guinier and Porod regimes), there are a series of cautions that necessarily need to be considered in order to correctly determine the polydispersity of a real sample from an experimental SAXS pattern. For instance, if the studied sample is highly diluted, the collected scattered intensities coming from the smallest particles will have poor data statistics, especially at intermediate- and high- $q$  values [3, 21, 22]. As a consequence statistical weight will be skewed to those

**Table 2.2** Most commonly used probability density functions to represent the polydispersity in nanoparticulate samples

Lognormal	$f(r) = \frac{1}{\sigma r \sqrt{2\pi}} e^{-\ln(r/r_0)^2/2\sigma^2}$	Being $\sigma$ the lognormal standard deviation and $r_0$ the mean particle radius
Gaussian	$g(r) = \frac{1}{\sigma \sqrt{2\pi}} e^{-(r-r_0)^2/2\sigma^2}$	Being $\sigma$ the standard deviation and $r_0$ the mean particle radius
Schultz-Zimm	$n(r) = \frac{[(z+1)/r_0]^{(z+1)} r^z}{\Gamma(z+1)} e^{-[(z+1)/r_0]r}$	Being $z = (r/\sigma)^2 - 1$ , $r_0$ the number-averaged radius, and $\sigma$ the root-mean-square deviation. $\Gamma$ being the gamma function

**Fig. 2.7** Experimental scattering curves from non-aggregate gold nanoparticles recorded at exposure times of 5 s (red curve) and 240 s (black curve)

particles of larger sizes. Experimentally, this obstacle can be addressed by increasing the exposure time ( $\tau_E$ ), i.e., the time in which the X-ray beam illuminates the sample and the detectors are counting photons. However, one needs to be cautious with the increase of  $\tau_E$ ; larger values of this could lead to saturation of the detectors,<sup>3</sup> thereby losing information or inducing serious damage to them [23]. Figure 2.7 presents two experimental SAXS patterns collected from colloidal gold nanoparticles (of spherical shape and  $\sim 5$  nm as the mean size). As can be perceived, the scattering intensity curve recorded with an exposure time of 5 s is noisier in almost the whole measuring range. However, by increasing the exposure time, until 240 s in this case, the statistical quality of the scattered signal was improved, making this curve a better candidate to be modeled.

Data collection time must be adjusted based on the nature of the sample and taking into account the radiation source. For instance, to examine the superatomic

<sup>3</sup>Every detector has a specific saturation value expressed in counts [2].

structure of biological samples, such as proteins, it is required to use radiation sources with high photon flux. If the X-ray radiation is extremely intense, as those coming from a synchrotron source ( $\sim 10^{11}$  photons per second), exposure times ranging between few seconds and 1 or 2 min are used. If the SAXS experiment is performed employing X-ray sources with smaller photon flux instead (benchtop devices or as those sources placed on crystallography laboratories), it will be necessary to increase the data collection time in order to obtain an optimal SAXS pattern.

### 2.3 Diluted Sets of Nano-objects: Experimental Data Modeling Assuming a Known Particle Shape

From a SAXS point of view, to catalog a system as diluted, it is necessary to ensure that the relative distances between particles are greater than their diameter. On the contrary case, the scattering intensity is affected by interference effects, and it will therefore contain contributions from neighboring particles. The simplest way to confirm that a system is diluted is to examine the scattering pattern linearity at the Guinier region (Sect. 2.2.2.1). If the diluted condition is satisfied, one can say that spatially uncorrelated objects compose the sample. Under this condition the total scattering intensity is given by  $I(q) = NI_p(q)$ ; recalling Eq. 2.10, here  $N$  represents the number of particles per unit volume, and  $I_p(q)$  is the scattering intensity of a single particle.

#### 2.3.1 Dilute Sets of Uncorrelated Spherical Nanoparticles

The simplest case is to assume a set of monodisperse spherical particles of radius  $R$  with constant electronic density  $\rho_P$ , which are embedded in a homogeneous matrix (e.g., colloidal, solid dispersion, or polymeric matrices), whose electronic density is also constant ( $\rho_M$ ). In this context, the total scattering intensity ( $I(q)$ ) can be obtained by solving the following equation:

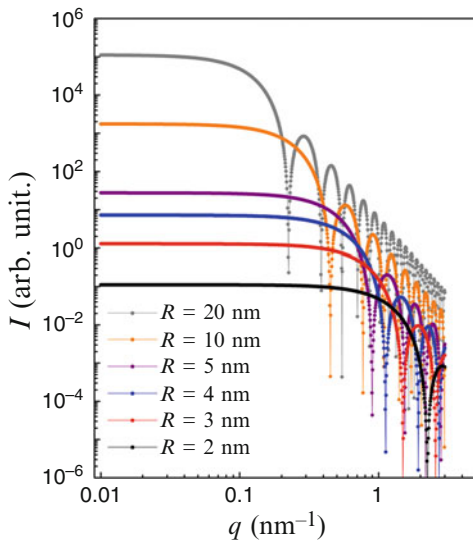
$$I(q) = N \left[ \Delta\rho \int_0^R 4\pi r^2 \frac{\sin(qr)}{qr} dr \right]^2, \quad (2.19)$$

whose solution for the particular case of monodisperse spheres, according to several references, including [17, 18], is:

$$I(q) = N(\Delta\rho)^2 V_P^2 3 \left[ \frac{\sin(qR) - qr \cos(qR)}{(qR)^3} \right]^2 \quad (2.20)$$



**Fig. 2.8** Simulated SAXS curves for monodisperse spherical particles constructed following Eq. 2.20 and varying radius



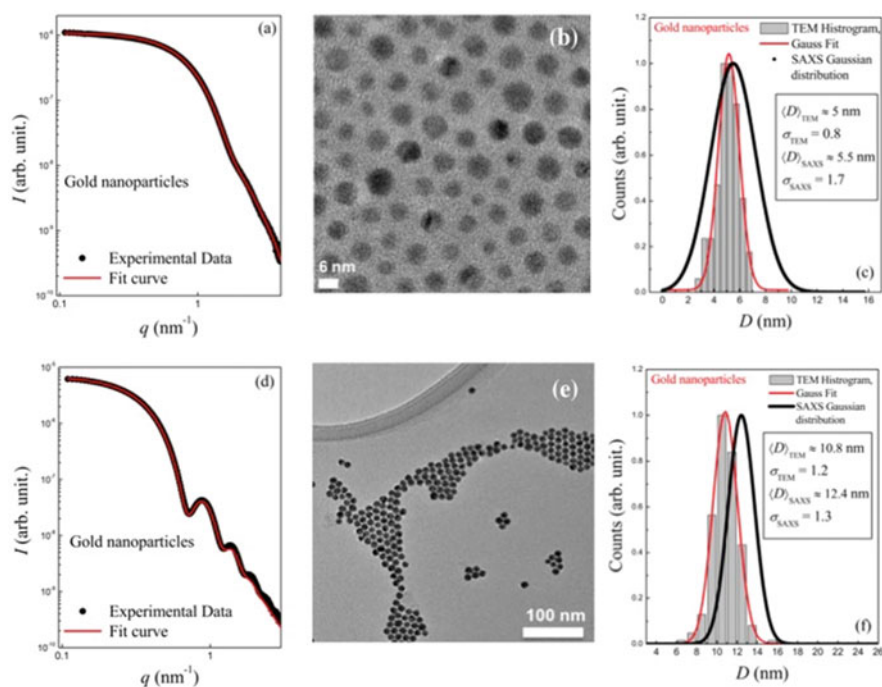
Here, the factor  $3 \left[ \frac{\sin(qR) - qR \cos(qR)}{(qR)^3} \right]^2$  is the form factor or the amplitude form factor for particles with spherical morphology  $P(q)$ ,  $\Delta\rho$  is the electronic density difference between the particles and the surrounding medium ( $\rho_P - \rho_M$ ), and  $V_P$  is the particle volume. Figure 2.8 displays a series of simulated SAXS curves constructed following Eq. 2.20 and assuming different radius ranging between 2 and 20 nm. In all curves the same tendency is evidenced, a linear trend at the Guinier region followed by an oscillatory behavior at intermediate- $q$  values.

As already mentioned, a nanoparticulate system can rarely be classified as monodisperse. On the contrary, most of the times, it presents polydispersity. This behavior can be examined knowing the polydispersity nature (lognormal, Gaussian, among others) or proposing a distribution function to model it. Under this circumstance, the total scattering intensity cannot be expressed as the sum of the individual contribution of each identical particle; rather particles with different size must be considered. Thus, the total scattering from a set of polydisperse particles is given by  $I(q) = \int N(r)I_p(q, r)dr$ , where  $N(r)$  symbolizes a proper distribution function (some of these are listed in Table 2.2). Notice that the scattering intensity of a single particle not only depends on  $q$  (or the angle) but also of their specific size. Following the same protocol used for monodisperse spheres, an expression to determine the total scattering can be achieved, resulting in:

$$I(q) = N(\Delta\rho)^2 \int_0^\infty V_P^2 \left[ 3 \frac{\sin(qr) - qr \cos(qr)}{(qr)^3} \right]^2 N(r) dr \quad (2.21)$$

### 2.3.1.1 Application of the Model That Describes the Scattering Intensity of Uncorrelated Spherical Nanoparticles: Gold Nanoparticles Diluted on Organic Solvents

Following the model discussed above, we have fitted two experimental SAXS curves obtained from a set of non-aggregated gold nanoparticles. Experimental (black curve) and fitted (red curve) results are presented in Fig. 2.9a, d. To test the scope of this model, none of the parameters involved in the model was restricted. Those structure parameters, derived from the SAXS fitted results, show an excellent agreement to those obtained by a direct method, like the transmission electron microscopy (TEM) (Fig. 2.9b, e). The small differences in the mean size as well as in the standard deviation can be linked to several causes, for example, the statistical contribution associated to each technique. While from TEM the counts are limited to hundreds or in the best of the cases to a few thousands of particles, from SAXS the illuminated portion of the sample may contain  $\sim 10^{12}$  particles or even more. The quality of the SAXS data, especially at high- $q$  values may generate errors in the obtained distribution. Furthermore, polydispersity errors are extremely sensitive to increasing particle interaction [24].



**Fig. 2.9** Experimental SAXS curves, TEM images, SAXS and TEM size distribution functions from non-aggregate gold nanoparticles with diameters of  $\sim 5$  nm (a–c) and  $\sim 12$  nm. SAXS fitted curves are presented as red continuous lines. Both TEM histograms were obtained by counting more than 500 particles from several TEM images

### 2.3.2 Dilute Sets of Uncorrelated Nanoparticles of Simple Geometrical Shape

A direct and simple approach to model a scattering curve is by starting from the knowledge or assumption of the particle shape. In Table. 2.3 some expressions for scattering intensity of particles with simple shapes are listed. Also, simulated SAXS patterns under specific geometrical considerations are displayed.

As can be noted, this approach is very useful if the shape of the scattering objects is known. Also, with this approach, it is possible to combine contributions from particles of different shapes, e.g., if the studied sample contains more than one family of objects with different shapes. Moreover, there are several form factors for complex morphologies, including core/shell spheres, bilayered or multilayered vesicle, and core/shell structures of elliptical or cylindrical shape [25, 26], among others. Some of this form factors have been successfully employed to characterize the growth of rare earth multilayers in magnetic nanoparticles [27] or well to analyze the size and shape effects on several physicochemical properties of the iron oxide nanoparticles [28]. The use of an analytical expression has numerous advantages; perhaps one of the most relevant is the reduced number of parameters, which make this approach a convenient tool to fit experimental data at low computational cost.

There are several cases where the irregular geometry of the scattering objects is difficult in the analytical calculation and the fitting process. Under this circumstance it is possible to use a method to approximate the particle geometry using subparticle units, whose shape may be spherical, elliptical, or cylindrical [29]. This approach packs small simple geometrical subunits to construct more complex ones [30]. For instance, the construction of these complex structures from spherical subunits can be done from finite element methods, to use then the Debye formulation to determine the intensity [5]:


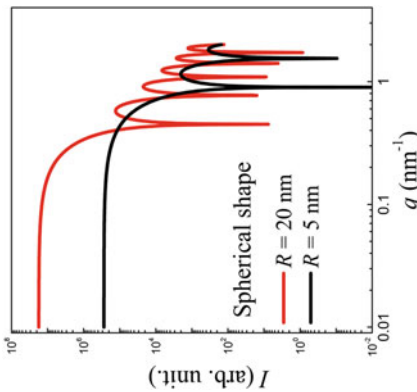
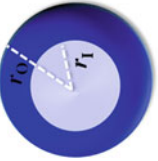
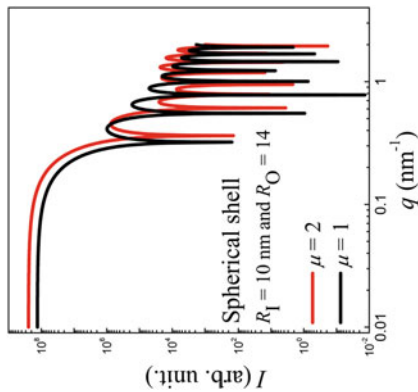
$$I(q) = \sum_{i,j=1}^N f_i(q)f_j(q) \frac{\sin(qr_{ij})}{qr_{ij}} \quad (2.22)$$


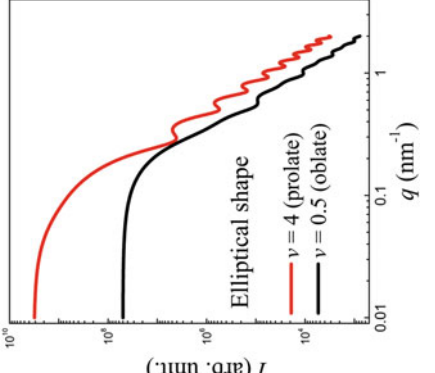

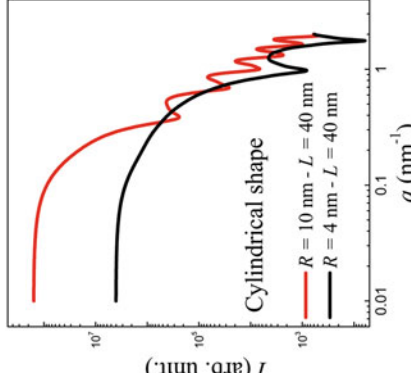
where  $N$  is the number of scattering particles,  $r_{ij}$  is the distance between atoms  $i$  and  $j$ , and  $f_i(q)$  is the scattering factor for atom  $i$ . This approach allows the calculation and optimization of complex systems admitting, if necessary, the use of additional terms to take into account possible particle interaction effects [31, 32].

## 2.4 Densely Packed Sets of Particles: Correlated Particles

The approaches discussed in the previous section have been founded on a common underlying assumption, which is that the investigated system is composed by diluted particles hosted in a matrix. Fundamentally, this means that the particle spatial

**Table 2.3** Expressions for the scattering intensity determined from particles of simple geometrical shape

Shape	Scattering intensity	Calculated SAXS pattern
Sphere of radius $R$	 $I(q) = N(\Delta\rho)^2 V_P^2 3 \left[ \frac{\sin(qR) - qR \cos(qR)}{(qR)^3} \right]^2$	 <p>Spherical shape</p> <ul style="list-style-type: none"> <li><math>R = 20</math> nm</li> <li><math>R = 5</math> nm</li> </ul>
Spherical shell with an inner radius $r_1$ and outer radius $r_0$	 $I(q) = [P(q, r_0, \Delta\eta) - P(q, r_1, \Delta\eta(1 - \mu))]^2$ <p>with</p> $P(q, r, \Delta\eta) = \frac{4}{3} \pi r^3 \Delta\eta^3 \left[ \frac{\sin(qr) - qr \cos(qr)}{(qr)^3} \right]$	 <p>Spherical shell</p> <ul style="list-style-type: none"> <li><math>r_1 = 10</math> nm and <math>r_0 = 14</math> nm</li> <li><math>\mu = 2</math></li> <li><math>\mu = 1</math></li> </ul>

<p>Ellipsoid of two equal semiaxis of length <math>r</math> and semiprincipal axis of length <math>\nu r</math></p>		$I(q) = (\Delta\rho)^2 \left(\frac{4}{3}\pi R^3\right)^{2\pi/L^2} \int_0^{2\pi/L^2} P^2(q, r(\nu^2 \cos^2\theta + \sin^2\theta)^{1/2}) \sin\theta \, d\theta$	
<p>Cylinder of radius <math>r</math> and length <math>L</math></p>		$I(q) = \frac{16(\pi R^2 L)^2 (\Delta\rho)^2 \int_0^q J_1(qR\sqrt{1-x^2}) \sin(qLx/2) dx}{q^2 R \sqrt{1-x^2} L x}$	

*Spherical shell*, scattering length difference between core and matrix relative to the shell contrast  $\mu$ . *Ellipsoid*, if  $\nu < 1$  the ellipse is oblate, and for  $\nu > 1$  the ellipse is prolate. *Cylinder*,  $J$  is the cylindrical Bessel function. All of the patterns were constructed assuming a monodisperse system. The expression listed here were adapted from reference [25]

arrangement effect on the total scattering intensity is negligible. However, in a densely packed system, the positions and orientations of their particles can be ordered or aligned following a preferential configuration, i.e., they can interact with each other [2]. Also, interacting particles can form clusters with a particular shape. Commonly, these systems are simply called *interacting* or *correlated*. A good example of these kinds of systems is those composed of magnetic or metallic nanoparticles, where the large surface/volume ratio plus intrinsic magnetic and/or ionic forces promotes the formation of clusters, as it is shown in these references [33–35]. The scattering intensity from this kind of systems not only carries the scattered information coming from a single particle but also contains the effects produced by the interference of those waves scattered by neighboring particles. To consider this additional interference, it is necessary to modify the scattering intensity expression determined from a set of non-correlated particles by adding the structure factor<sup>4</sup>  $S(q)$ , which contains the information about the spatial position of the particles.

The total scattering intensity for a system composed of  $N$  spatially correlated particles is given by:

$$I(q) = NI_p(q)S(q) \quad (2.23)$$

Recalling that  $I_p(q) = (\Delta\rho)^2 V_p^2 P(q)$ , with  $P(q)$  being the form factor (associated to the scattering amplitude  $A(q)$ ), then Eq. 2.23 can be rewritten as:

$$I(q) = NP(q)S(q) \quad (2.24)$$

Assuming that the particles are close to each other but non-percolated, the structure factor  $S(q)$  for a monodisperse system is given by [29]:

$$S(q) = 1 + \frac{N}{V} \int_0^\infty 4\pi r^2 (P(r) - 1) \frac{\sin(qr)}{qr} dr, \quad (2.25)$$

where  $P(r)$  is the pair-distribution function mentioned above and the integral  $\int_0^\infty 4\pi r^2 (P(r) - 1) \frac{\sin(qr)}{qr} dr$  is the Ornstein-Zernike integral, which is in fact the expression that carries the information of the pair distance among the particles in a system.

As mentioned before, the correlated effects between nanoparticles are particularly appreciable at the Guinier region (low- $q$  values) as shown in Fig. 2.4a. This can be analyzed well from the asymptotic behavior of  $S(q)$ . For instance, at high- $q$  values, this factor tends to be 1, while at low- $q$  values,  $S(q)$  exclusively depends on the nature of the interaction. Furthermore, it can be noticed that for a set of non-correlated particles,  $S(q)$  takes a value of 1, and thus Eq. 2.25 turns into Eq. 2.10.

---

<sup>4</sup>In crystallography it is known as the lattice factor.

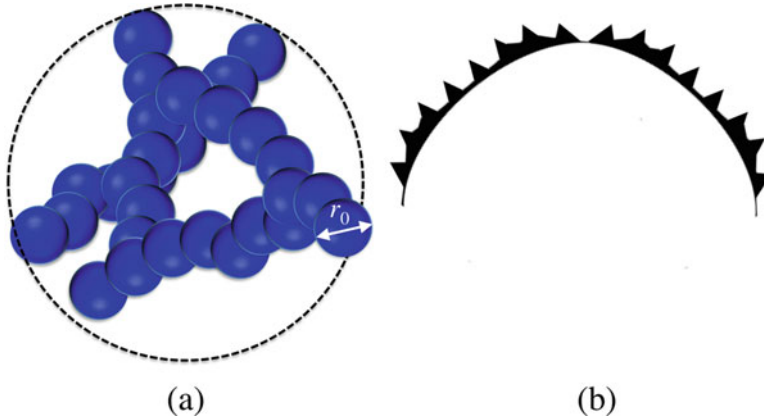
The solution of Eq. 2.25 depends on the nature of the interactions as well as on the type of the formed aggregate, i.e., of  $P(r)$ . When a structure factor is introduced in the scattering intensity equation, one tries to establish what kind of interaction potential is present in the sample. Some of the most used interaction potentials, developed for globular particles, are the hard sphere, the sticky hard sphere [36], the squared-well potential, or the rescaled mean spherical approximation (based on spheres with Coulomb interaction) [37]. To solve the Ornstein-Zernike integral, there must be a closure relationship between the correlation function and the potential [29]. Some of the most common closure relationships are the Percus-Yevick approximations [38], which have been successfully used to find an analytical solution for the Ornstein-Zernike integral for a hard sphere and sticky hard sphere potentials. There are several closure relations reported to solve the Ornstein-Zernike integral, such as the mean spherical approximation, the Roger-Young (RY) closure [39], and the zero separation theorem-based closure (ZSEP) [40], among others. A complete list can be consulted in reference [25]. Once it is determined, which potential will be employed and the respective closure relation, the Ornstein-Zernike integral equation can be solved, and thus the correlation function can be obtained. Then, the structure factor is determined by using Eq. 2.25. This methodology can be followed to introduce other interaction forms as well as to insert, if necessary, suitable size distribution functions.

In this chapter, our objective is not focused on analyzing the solutions of the Ornstein-Zernike integral from different closure relations or demonstrating how some structure factors are obtained; rather we will focus our efforts on two particular approaches often employed to obtain valuable information from experimental data obtained from a nanoparticulate system. These are the fractal aggregate model and the unified exponential power law model (Beaucage model).

### 2.4.1 Fractal Aggregate Model

The fractal aggregate model (FA) was postulated by Chen and Teixeira in the mid-1980s [41], since then it has been widely applied to investigate structural features of diverse systems, including biological and nanoparticulated systems. Particularly speaking of nanoparticulated materials, the aggregation dynamics is related to the nature of the nanoparticle components. For example, metallic nanoparticles, such as silver or gold, hosted in water tend to form aggregates due to ionic forces, while for magnetic nanostructures, including nanoparticles of iron, cobalt, nickel, or their respective oxides, magnetic interaction can promote the formation of aggregates [42]. In these two cases, the interacting forces depend on several factors, such as the size of the nanoparticles, the polarity of the host solvent, and the nanoparticle functionalization, among others.

The application of the FA model for correlated nanoparticles has been founded assuming that  $N$  primary nanoparticles (of radius  $r_0$ ) can be spatially arranged



**Fig. 2.10** (a) Schematic representation of a mass fractal structure. This structure is made out of primary particles of radius  $r_0$  that are aggregated. (b) Schematic representation of a surface fractal structure of moderated roughness

forming aggregates of mass  $M$  and size  $\xi$ . These quantities are directly related through a power law, as follows:

$$M \sim \xi^{D_F} \quad (2.26)$$

where  $D_F$  is the fractal dimension that depends on the nature of the aggregation mechanism [6]. Those aggregates whose mass increase follows Eq. 2.26 are known as *mass fractals* [43]. A mass fractal aggregate can be understood as a large structure with branches cross-linked by the effect of certain forces, as is shown in Fig. 2.10a. Notice that the concept behind  $D_F$  is consistent with the common notion of Euclidean objects, i.e., for objects with homogeneous shapes, such as globular, planar, or elongated 1-D objects,  $D_F$  takes values of 3, 2, and 1 [44], respectively. While, for objects with mass fractal features,  $D_F$  takes semi-integer values. On the other hand, the surface of the aggregates can also have fractal topographies, in this case referred as *surface fractals* (see Fig. 2.10b). Here, the proportional relationship between fractal surface  $S$  and aggregate size  $\xi$  is given by:

$$S \sim \xi^{D_S} \quad (2.27)$$

where the exponent  $D_S$  carries the aggregate roughness information, being 2 for smooth surfaces and taking values ranging between 2 and 3 for surfaces with fractal topographies [9].

Using the above information, one can generalize the Porod law, which becomes:

$$I(q \rightarrow \infty) \sim q^{-2D_F + D_S} \quad (2.28)$$



Notice that for a globular aggregate ( $D_F = 3$ ) with smooth surface ( $D_F = 2$ ), the Porod law keeps its power dependence with  $q^{-4}$ .

Remembering, the structure factor  $S(q)$  for a set of correlated monodisperse nanoparticles can be determined by solving Eq. 2.25. Certainly this implies determining first a suitable pair-distribution function  $P(r)$ . Thus, one can start from the fact that the primary particle number density inside a sphere of radius  $r$  is given by [6, 9].

$$N(r) = (r/r_0)^{D_F} \quad (2.29)$$

Note that Eq. 2.29 is valid if the number of primary particles is calculated from the center of the mass fractal aggregate. Moreover, from the pair-distribution function definition, it is also possible to determine the primary particle number density [45], as follows:

$$N(r) = \frac{N}{V} \int_0^{\infty} 4\pi r^2 P(r) dr \quad (2.30)$$

From Eqs. 2.29 and 2.30, the following equivalence is reached:

$$(r/r_0)^{D_F} = \frac{N}{V} \int_0^{\infty} 4\pi r^2 P(r) dr \quad (2.31)$$

Then, Eq. 2.31 can be solved to find the expression for the pair-distribution function:

$$P(r) = \frac{1}{r_0^{D_F}} \frac{1}{4\pi N} D_F r^{D_F-3} \quad (2.32)$$

Finally, introducing the obtained result from the Eq. 2.32 into Eq. 2.25, and then solving it, the structure function for a fractal object is given by [45]:

$$S(q) = 1 + \frac{1}{(qr)^{D_F}} \frac{D_F \Gamma(D_F - 1)}{[1 + 1/(q\xi)^2]^{(D_F-1)/2}} \sin \left[ (D_F - 1) \tan^{-1}(q\xi) \right] \quad (2.33)$$

From the asymptotic behavior of Eq. 2.33, one can also find valuable information. For example, analyzing the expression at the Guinier region ( $S(q \rightarrow 0)$ ), one can find an expression for the radius of gyration of the mass fractal aggregate:

$$R_g^2 = \frac{D_F (D_F + 1) \xi^2}{2} \quad (2.34)$$

A complete procedure to obtain the radius of gyration of the mass fractal is available in [9, 45].

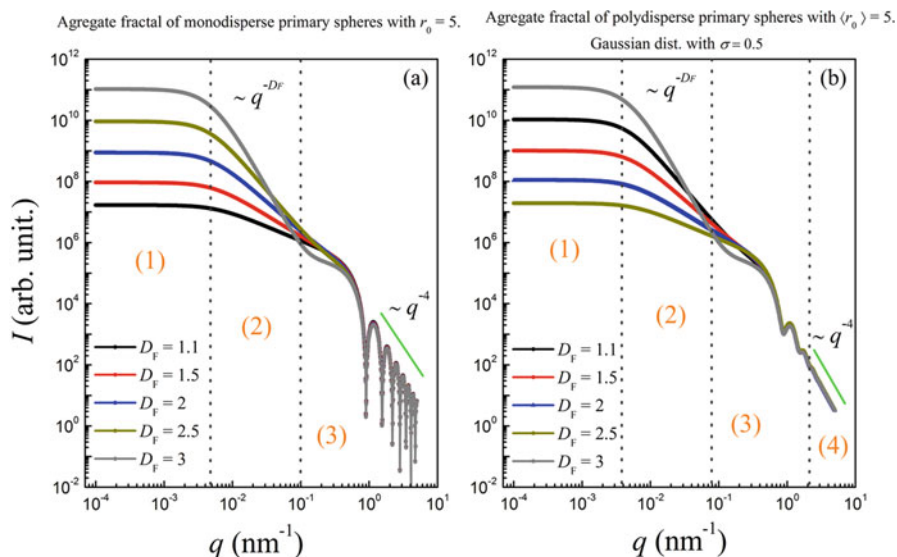
In the case of a system composed by monodisperse correlated nanoparticles, one can select the sphere form factor (listed in Table. 2.3) and thus apply Eq. 2.24 ( $I(q) \sim P(q)S(q)$ ) to finally determinate an expression for the scattering intensity produced by a system with fractal aggregate architecture, which is:

$$I(q) = N(\Delta\rho)^2 V_P^2 3 \left[ \frac{\sin(qr_0) - qr_0 \cos(qr_0)}{(qr_0)^3} \right]^2 \left\{ 1 + \frac{1}{(qr_0)^{D_F}} \frac{D_F \Gamma(D_F - 1)}{[1 + 1/(q\xi)^2]^{(D_F-1)/2}} \sin[(D_F - 1) \tan^{-1}(q\xi)] \right\} \quad (2.35)$$

being  $\Gamma$  the gamma function. For systems composed by polydisperse correlated nanoparticles, it is necessary to introduce a suitable distribution function  $f(r)$  to then integrate the expression  $I(q) \sim \int P(q)S(q)f(r)dr$ .

In Fig. 2.11 we present a series of representative SAXS curves of fractal structures composed by primary particles of spherical shape. To construct Fig. 2.11a, we decided to carry out the simulation keeping constant two of the structural parameters,  $r_0$  and  $\xi$ , but varying the fractal dimension  $D_F$ . On simulation displayed in Fig. 2.11b, a Gaussian size distribution  $g(r)$  was introduced in order to consider the polydispersity effect. Also,  $r_0$  and  $\xi$  were kept constant, while  $D_F$  was changed, choosing values ranging between 1.1 and 3. On these figures, one can see different characteristic regions. Notice that for the fractal structures constructed with monodisperse spheres, the Porod trend (at high- $q$  values) is screened, because the SAXS intensity exhibits the oscillatory behavior even at large- $q$  values. Each region carries specific information. This means:

1. The first region, defined for the small- $q$  range ( $q \ll \xi$ ), is known as the Guinier region for the aggregate. For this  $q$  range,  $I(q)$  behaves accordingly to the Guinier law. Note that depending on the aggregate size, it becomes necessary to record the scattering intensity at extremely small- $q$  values, which from an experimental point of view represents a big challenge. From this region it is possible to determine the aggregate size as well as their radius of gyration (Eq. 2.34).
2. The second region is described over the intermediate- $q$  region and can be defined when  $1/\xi < q < 1/r_0$ . In this region the scattering intensity falls, following a power



**Fig. 2.11** Simulated SAXS curves according to the FA model for a set of (a) monodisperse and (b) polydisperse nanoparticles. For each five SAXS curves were simulated varying the fractal dimension

law of  $I(q) \sim q^{D_F}$ . Since this region comprises the aggregated Porod zone and the primary particle Guinier zone, then the fractal dimension of the aggregate and the size of the primary particles can be determined.

3. The third region or the oscillatory one is defined at  $q > 2/r_0$ . Since this oscillatory behavior is related to the size distribution of the primary particles, one can determine the degree of polydispersity of the primary particles.
4. Finally, the last region, better defined in Fig. 2.11b, describes the scattering intensity behavior at large- $q$  values. This is associated to the Porod zone of the primary particles, which means that the scattering intensity decreases following a power law of  $I(q) \sim q^{-4}$ .

There are several papers where this model is applied in order to determine the most important structural parameters linked to the formation of aggregates. Specially, when working with magnetic nanoparticles, it is extremely important to take them into account, since their degree of aggregation and the aggregate features can modify the macroscopic magnetic response of the system. Some examples of this behavior can be found in these references [27, 33–35, 46].

On Sect. 2.4.3 we will present some examples where this model is applied in order to structurally characterize nanoparticulated systems.

### 2.4.2 Unified Exponential/Power Law Model (Beaucage Model Based on Hierarchical Structures)

The unified exponential/power law model postulated by Beaucage describes the scattering intensity produced by an aggregate of fractal dimension  $D_F$  and radius of gyration  $R_g$  [47]. Basically, this model combines the Guinier and Porod regimes into a unified expression to describe the scattering intensity behavior of any morphology of complex systems containing multiple levels of related structural features [34, 35, 47, 48]. As in the FA model, the aggregates are considered as constituted by single subunits (primary particles), which has a radius of gyration  $r_S$ . This model establishes a semiempirical expression for  $I(q)$ . For two structural levels (aggregates and single subunits), the equation for  $I(q)$  is given by:

$$I(q) = G \exp \left[ -\frac{q^2 R_g^2}{3} \right] + B \exp \left[ -\frac{q^2 r_S^2}{3} \right] \left( \left[ \operatorname{erf} \left( \frac{q R_g}{\sqrt{6}} \right) \right]^3 / q \right)^{D_F} + G_S \exp \left[ -\frac{q^2 r_S^2}{3} \right] + B_S \left( \left[ \operatorname{erf} \left( \frac{q r_S}{\sqrt{6}} \right) \right]^3 / q \right)^P \quad (2.36)$$

where erf is the error function and  $P$  is the Porod exponent, which usually takes a value of 4.  $G$  and  $B$  are, respectively, the Guinier and Porod pre-factors for the aggregate, while  $G_S$  and  $B_S$  are the respective pre-factors for the primary particles. Thus, the first term describes the aggregate structure, while the second one carries the information of the mass fractal structure [25]. The last two terms contain the structural information of the single subunits. For aggregates formed by solid particles of globular form, the mentioned pre-factors are given by [34, 44]:

$$G = N_\xi \Delta \eta^2 \left( \frac{4\pi}{3} \right)^2 \left( \frac{\xi}{2} \right)^6 \quad (2.37)$$

$$B = 2\pi N_{PP} \Delta \eta^2 S \quad (2.38)$$

$$G_S = N_{PP} \Delta \eta^2 \left( \frac{4\pi}{3} \right)^2 r_S^6 \quad (2.39)$$

$$B_S = 8\pi N_{PP} \Delta \eta^2 r_S^2 \quad (2.40)$$

being  $N_\xi$  the number of aggregates per unit volume,  $\Delta\eta$  the scattering length density difference between the particles and the host matrix,  $N_{pp}$  the number of small subunits within each aggregate, and  $S$  the specific surface. For a set of experimental SAXS data, one can use Eq. 2.36 to fit the data and obtain the three parameters of importance, being these  $\xi$ ,  $r_s$ , and  $D_F$ . With these information, other valuable structural information can be indirectly obtained, for example, the number of aggregates per unit volume  $N_\xi$  [34]:

$$N_\xi = \frac{G}{\Delta\eta^2 \left(\frac{4\pi}{3}\right)^2 \left(\frac{\xi}{2}\right)^6} \quad (2.41)$$

Besides, if the aggregate is composed by polydisperse single primary particles, the structural parameters involved in Eqs. 2.37–2.40 can be replaced by their averaged expressions, i.e.,  $\xi$  and  $r_s$  can be substituted by  $\langle\xi\rangle$  and  $\langle r_s\rangle$ , respectively. According to Ref. [44], the averaged expressions can be merged to determine the polydispersity index (PI) of the primary particles, resulting in:

$$PI = \frac{B_S r_S^4}{1.62 G_S} \quad (2.42)$$

being  $PI = 1$  for monodisperse primary particles.

As can be noted, the approach above discussed has been founded on the assumption that the investigated system contains two structural levels (aggregates and primary particles). However, the Beaucage model can also be extended to describe the scattering intensity of an arbitrary number or structural levels [25]; thus Eq. 2.36 becomes:

$$I(q) \approx \sum_i^n \left[ G_i \exp \left[ -\frac{q^2 R_{g,i}^2}{3} \right] + B_i \exp \left[ -\frac{q^2 R_{g,i+1}^2}{3} \right] \left( \left[ \operatorname{erf} \left( \frac{q R_{g,i}}{\sqrt{6}} \right) \right]^3 / q \right)^{P_i} \right] \quad (2.43)$$

where  $n$  is related to the number of structural levels and being  $i = 1$  for the largest one.

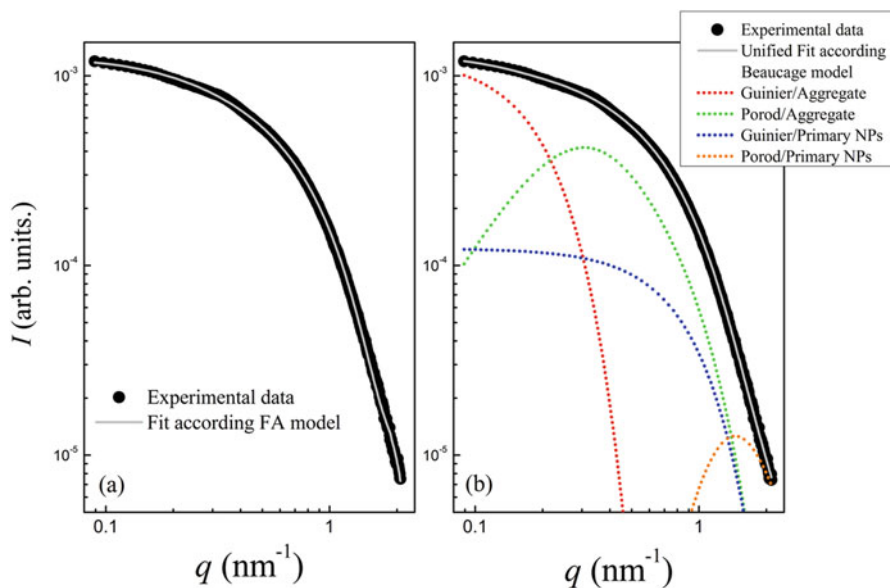
In the next section, we will present some examples where the Beaucage model is applied to structurally characterize systems conformed by nanoparticles hosted in colloids or in solid polymeric matrices.

### 2.4.3 *Application of the Fractal Aggregate and Beaucage Models on Specific Systems with Correlated Nanoparticles*

In this section we will show the application of the FA and Beaucage models on particular samples. The samples presented here were synthesized by our research group. For the first example (colloidal silver nanoparticles), the SAXS patterns were recorded in the Brazilian Synchrotron Light Laboratory while for the second example (Fe oxide nanoparticles loaded in polymeric matrices) already published in [34]. Essentially, we will focus in analyzing the most important regions of the SAXS pattern, as well as in briefly discussing the most interesting results.

#### 2.4.3.1 **Correlated Nanoparticles: Silver Nanoparticles Diluted on Organic Solvent**

The Ag nanoparticles studied here were prepared following the thermal-assisted reduction procedure. According to TEM images (not shown here), the nanoparticles present a moderate aggregation degree, and their sizes are framed in a lognormal-type distribution with a mean diameter of  $\sim 4$  nm. According to the experimental SAXS pattern, displayed in Fig. 2.12 (black symbols), the scattering intensity follows a power-law behavior for the low- $q$  range instead of the Guinier behavior; this is a first signal of the existence of nanometric scale aggregates. In the intermediate- $q$  region ( $0.16 \text{ nm}^{-1} < q < 0.26 \text{ nm}^{-1}$ ), the scattering intensity seems to follow a power law dependence with  $\sim q^\alpha$  (with  $\alpha = 2$ ) suggesting the presence of aggregates with a fractal structure. After this region, the absence of an oscillatory behavior confirms the existence of a size distribution of moderate width. For the high- $q$  values (Porod region), the scattering intensity falls according to a power law of  $\sim q^{-4}$ , characteristic of elementary particles with smooth surface. This first semiquantitative analysis leads us to think that a model of correlated particles must be applied in order to get the suitable structural information. In that sense, we decide to use the previously discussed model to fit the experimental data. Figure 2.12a, b shows the fitting results by following the FA and Beaucage models. According to the results, from the FA model, a mean primary diameter of  $\sim 4.1$  nm and a fractal dimension  $D_F$  of  $\sim 1.90$  were obtained, while following the Beaucage expression, values of 4.4 nm and 1.92 were calculated for primary particle diameter and fractal dimension, respectively. Comparing the values obtained from both models, one can note that the slight differences are in the same magnitude order than the experimental error. Thus, it can be concluded that the two employed models are suitable to obtain the desired morphological information. It is noteworthy that the primary particle size determined from both approaches is in good agreement to those obtained from microscopy techniques. These results suggest the formation of aggregates with a two-dimensional structure. The size of this structure was directly obtained from the FA model, being  $\xi \approx 14$  nm. Despite that from the



**Fig. 2.12** Experimental SAXS pattern (black symbols) obtained from a set of silver colloidal nanoparticles. (a) Best fitting results according to the fractal aggregate model. (b) Best fitting result following the extended Beaucage expression described in the text. Contribution of the Guinier and Porod for aggregates and primary particles are presented as dotted lines

**Table 2.4** Structural information derived from the fitting procedure according to the FA and Beaucage models

FA model				Beaucage model			
$\langle D \rangle$ (nm)	$\sigma$	$\xi$ (nm)	$D_F$	$D_S$ (nm)	$D_F$	$R_g$ (nm)	$D_{Agg}$ (nm)
$\sim 4.1$	0.2	$\sim 14$	1.96	$\sim 4.4$	2.01	$\sim 14.8$	$\sim 11$

$D_S$  was calculated using  $D_S = 2r_s$ .  $D_{Agg}$  is the aggregate diameter; this was indirectly determined using the radii of gyration ( $R_g$ ) of the aggregates and assuming their 2-D morphology as something close to a thin circular disk with radius  $R$  ( $R_g^2 = \frac{R^2}{2}$ ), i.e.,  $\frac{D_{Agg}}{2} = (2R_g)^{1/2}$

Beaucage model the aggregate size cannot be directly obtained, we assume a 2-D structure, with a morphology similar to a thin circular disk. Under this assumption the aggregate size was determined, obtaining a value of approximately 11 nm. A complete list with the fitting results is presented in Table 2.4.

### 2.4.3.2 Correlated Iron Oxide Nanoparticles Loaded in Nonconducting Polymeric Matrices: The Role of the Nanoparticle Concentration

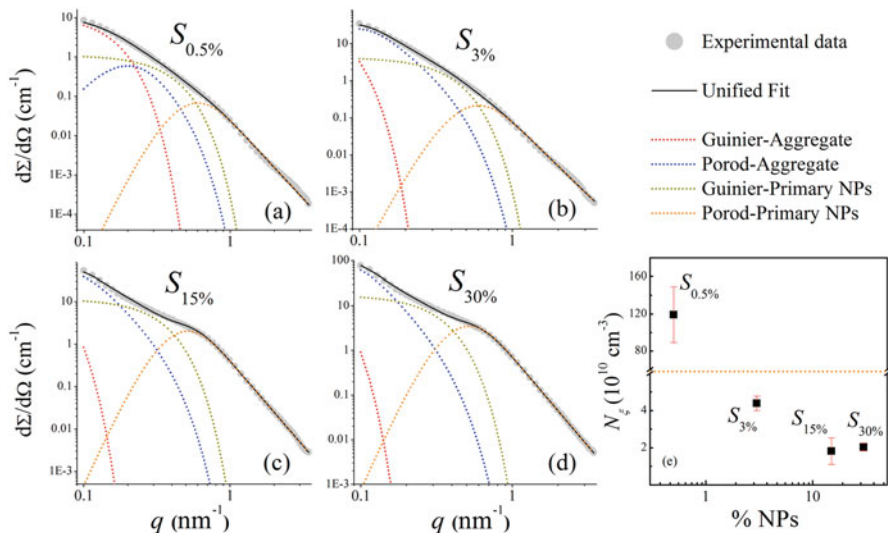
With this example we show how the previously discussed models (Sects. 2.4.1 and 2.4.2) can be applied to follow the nanoparticle agglomeration degree on

magnetic polymer nanocomposites. With this intention we have retaken part of a work already published [34] but solely focused the discussion on the most relevant information obtained from the SAXS technique. According to the mentioned work, the studied samples are prepared by loading four different concentrations of iron oxide nanoparticles (0.5 wt.%, 3 wt.%, 15 wt.%, and 30 wt.%) on polymeric matrices of polyvinyl alcohol (PVA). Synthesis details can be consulted on [34].

Regarding the cited work, the SAXS intensities were well fitted following the extended Beaucage expression for two structural levels (Eq. 2.36). Among the most important results, this work stresses that the aggregate size ( $\xi$ ) and the fractal dimension ( $D_F$ ) increase as the nanoparticle concentration rises, indicating the formation of larger and most compact aggregates for those systems with larger amounts of Fe oxide nanoparticles. These features are reflected also on their magnetic properties [49] (Fig. 2.13).

## 2.5 Small-Angle X-Ray Scattering Instrumentation

An X-ray source, a collimation system, a sample holder, a beam stopper, and a detection system basically compose every SAXS instrument. In a typical experiment, the sample is irradiated by a very narrow, collimated beam of fixed diameter, and the elastic, coherent scattered radiation is detected at very low angles, requiring in first



**Fig. 2.13** (a–d) SAXS curves of the magnetic composites. The experimental data represented by symbols. Guinier and Porod contributions for the two structural levels are presented as dotted lines. (e) Number density of magnetic aggregates ( $N_\xi$ ) as a function of nanoparticle concentration (Figure repeated with permission from [34])



instance that the detector is placed a few meters away from the sample, since the scattered intensity decays as the inverse of the squared distance. It is noteworthy that the main instrumental challenge is separating the weak scattered radiation from the strong main beam, which travels through the sample and reaches the detector directly, making the beam stop indispensable.

The *X-ray source* constrains the entire equipment design and construction; it divides the instruments in two big groups, the laboratory or benchtop SAXS instruments, equipped with conventional X-ray sources, e.g., X-ray tubes of the characteristic wavelength of the anode material [5]. Secondly, the synchrotron SAXS instruments obtain X-rays from the electromagnetic radiation emitted from charges accelerated at relativistic velocities, usually electrons or positrons. These instruments combine great advantages like high intensity, narrow angular divergence, and broad spectral range, extending the possibilities of SAXS applications [1], e.g., time-resolved and anomalous SAXS measurements.

A second classification of the instruments can be done regarding the collimation mechanism, which must contemplate two main challenges: the beam size, directly related to the resolution, which must be balanced by larger divergence to ensure sufficient intensity and the parasitic scattering caused by the process of beam reduction, which must be minimized. A high-power density of an incident X-ray beam will be a waste if these aspects are ignored [50]. Three main classes of instruments can be defined:

- (a) Slit-collimated instruments: using parallel slits is the simplest and reasonably the first historically employed solution to collimate a SAXS instrument beam. The resolution can be improved with narrower slits and longer inter-slit distances, but it is limited by the parasitic scattering emitted at low angles. The latter can be avoided introducing additional slits in the appropriate configuration. In these instruments, also known as Kratky cameras, the primary beam is usually emitted with a line-shaped cross section; hence the superposition of intensity contributions from various scattering points along the line-shaped beam can occur, causing distorted or blurred patterns that must be properly corrected before being analyzed.
- (b) Pinhole-collimated instruments: the growing technological development of point-source X-ray generators as well as 2-D focusing optics augmented the popularity of these instruments over slit-collimated, due to sample versatility and easy availability of data reduction and analysis procedures. In a pinhole-collimated instrument, the pinhole selects a highly coherent part of the beam and produces a finite illumination area, with a circular or elliptical shape. Thus, the scattering pattern is a centrosymmetrical distribution formed by concentric circles around the illuminated spot of the primary beam, useful for investigations on orientation distributions.

Compared to slit-collimated instruments, the illuminated volume in the sample is small and so will be the scattered intensity, comprising the resolution. The latter can be improved increasing the sample-to-detector distance, resulting

in larger instruments (up to few meters) and lower intensity at the detector, increasing the needed measurement time up to hours.

- (c) Bonse-Hart instruments: taking advantage of the high angular selectivity of crystalline reflections, an intense, large cross-sectional X-ray beam, with very small angular divergence, can be obtained. For this purpose a first fixed crystal is placed between the source and the sample to collimate the incident beam, so that the radiation from the source strikes it at the Bragg angle. A second rotatable crystal placed after the sample is responsible for the analysis of the angular distribution of the scattered radiation, since the highest reflectivity is only for radiation impinging upon it at the Bragg angle [51]. The novelty introduced by Bonse and Hart was an increase in the angular resolution by increasing the number of reflections in each of the crystals, preserving the main beam intensity and reducing its tails [52]. With conventional X-ray sources, these instruments have low efficiency in the mid- $q$  range, because the point-taking technique excludes the use of position-sensitive detectors, limiting these instruments to systems of rather large scatterers. Conversely, the point-by-point measurement limitations can be compensated using higher flux synchrotron radiation [53]. A third crystal may be added parallel to the second, expecting to diminish even more the beam tails.

The *sample holder* is a key component of the instrument; it must be versatile enough to adapt to many sample preparations and SAXS modes, i.e., transmission mode and reflection/grazing angle (GISAXS). The sample-to-detector beam path should be free of scatterers to minimize background scattering, this includes air molecules, and hence vacuum is required ideally. In most experiments, samples are destroyed when subjected to vacuum conditions and require control over parameters such as temperature, pressure, flow/shear rate, humidity, strain, projection angle, etc. As a consequence, completely homemade or variants of commercially available sample holders are often used. Most common sample preparations are described in [2]:

- (a) Liquids are usually measured in transmission mode in thin-walled capillaries of variable thickness, according to the absorbance of the solvents, i.e., heavy atoms composed of solvents require thinner walls. Suspensions must be stable over time and sufficiently diluted.
- (b) Pastes, rubbers, powders, and vacuum-sensitive materials are usually mounted on sample holders of removable windows. A commonly used window material is a polyimide or a beryllium film, characterized for being transparent to X-rays, with high mechanical and thermal stability.
- (c) Solids can be fixed to frames; the same film can be used for protection and stabilization. Thickness must be controlled to ensure sufficient transmittance for the measurement.
- (d) Materials on a substrate can be measured on transmission mode if the substrate is sufficiently thin and X-ray transparent; otherwise it must be measured in reflection mode, as long as the thin film material scattering is stronger than the scattering of the substrate.

In many cases if samples require a controlled atmosphere or are sensitive to vacuum, they are placed in a small compartment that is inserted into the vacuum. It must be kept in mind that the windows and air or gas volume of this compartment can contribute to background scattering.

The *beam stop* is responsible for protecting the detection system of the direct intense main beam or the possible overhanding of the scattered signal caused by strong backscatter from the detector material when reached by the intense beam.

The main beam can be completely blocked with an opaque, dense material like lead or tungsten or attenuated with a transparent material to a manageable intensity. When attenuated, the main beam profile and the zero-angle position can be acquired directly in each measurement, but possible background scattering caused by the beam stop material must be taken into account. A third option is to substitute or condition the beam stop with a PIN diode in order to characterize the transmitted beam.

In X-ray free-electron lasers (XFEL), the focused primary X-ray beam has sufficient energy to ablate most materials; small primary beam stops cannot be used in front of the detectors, as is customary at storage ring sources. Therefore, the X-ray imaging detectors in the forward scattering direction need to have a central hole to let the direct beam through.

SAXS parameters of interest are the flux and position of the incident photons. The detection system employs a mechanism that absorbs the energy from an X-ray photon and transforms it into an electrical signal. Some of these mechanisms are the ionization of a gas, liquid, or solid; the excitation of optical states, known as scintillation; and the excitation of lattice vibrations (phonons).

To this aim, the most commonly employed detectors are [2]:

Wire detectors consist of one or an array of parallel wires to produce a 1-D or 2-D scattering patterns, respectively, placed inside an absorbing gas atmosphere (Xe or Ar/methane) in the presence of an applied high voltage bias. An entering X-ray photon ejects an electron from the gas molecules, which accelerates toward a wire and induces an electrical pulse that propagates in both directions of the wire. The arrival of the pulse to both of the wire ends is recorded, and the time difference can be related to the position where the impulse was generated. This technique has a rather poor spatial resolution but a high sensitivity to different wavelengths.

- (a) Charge-coupled device (CCD) detectors, like conventional cameras, detect visible light which is emitted from a fluorescence screen when an X-ray photon impacts. A glass fiber plate is placed between the screen and the video chip to conduce the light with minor distortions. Each pixel consists of a capacitor that charges with the incident radiation; hence no pulses can be filtered. The resolution and quality of the acquisition will be dependent on the number, size, and quality of the chips, on an efficient cooling system, and on the ability of on-chip binning, which interconnects chip information to increase the precision.
- (b) Imaging plates detectors consist of photostimulable composite structures (e.g., BaF(Br,I) Eu<sup>2+</sup> micrometer-sized crystals coating a plastic plate) capable of storing a fraction of the absorbed X-ray energy as excited electrons. Posterior

exposure to visible light liberates the stored energy as luminescence, proportional to the absorbed X-ray intensity. The photostimulated luminescence wavelength differs from that of the stimulating radiation and can be collected with photomultiplier tubes or avalanche photodiodes, amplified and converted to a digital image. The plate can be reused after exposed to visible light to remove any residual stored energy [54]. The resolution mainly depends on the readout system.

- (c) Solid-state detectors or CMOS (complementary metal-oxide-semiconductor) are based on a semiconductor crystal, commonly silicon or germanium, subjected to a bias. When an X-ray photon is absorbed, a number of electron-hole pairs are created proportional to the energy of the incident X-ray photon divided by the energy required to produce an electron-hole pair, reflected in high-energy resolution. The applied bias induces a current by the movement of the positive and negative charge carriers, and the charge, proportional to the energy of the incident photon, is collected.

The whole instrumental selection and design must be engineered to maximize the achievable resolution, defined by the length of the flight tube, the beam size and divergence, and the point spread function of the detector. It must be kept in mind that each of the components can originate pattern smearing as a consequence of effects like finite collimation, finite detector resolution, and wavelength spread. Equilibrium can be looked for between high-quality equipment (costs/facilities) and manageable data analysis.

### ***2.5.1 Small-Angle X-Ray Scattering and Transmission Electron Microscopy***

In the last section of this chapter, we want to highlight the importance of microscopy experiments as a complementary technique to determine the structure features in nanoparticulate systems. Both transmission electron microscopy (TEM) and small-angle X-ray scattering (SAXS) are the most used techniques to determine the morphology features of a set of nanoparticles. Both techniques (as well as others that use radiation) create an output signal by taking advantage of the electron density function difference between the studied objects and surrounding medium. Basically SAXS and TEM techniques are based on the same physical principle, but, at the end, the obtained information is recorded in a different way. For example, in microscopy the scattering pattern is treated by a set of lens, from which the image is reconstructed. Instead, in a SAXS experiment, the scattering pattern is recorded, and a potential image must be reconstructed mathematically.

Certainly TEM and SAXS have advantages and disadvantages. It is clear that the greatest advantage of TEM is the direct generation of real images of the studied object. However, this technique is restricted to a small portion of the sample, a fact that, for example, can limit the construction of an accuracy size distribution curve.

For nanoparticles composed of atoms of low molecular weight (such as carbon, sulfur, phosphorous, among others), it is also common to have problems identifying the nanoparticle boundaries. On the other hand, in the SAXS technique, a larger volume of the sample can be illuminated, a fact that leads to the estimation of more precisely average values. Despite that the SAXS pattern is obtained from over all particles oriented in all directions, the structural features are determined in an indirect way, an issue that could lead to ambiguous results and wrong interpretations. The previous facts indicate that in order to obtain a complete picture of the structural features at superatomic scale, it is recommendable to combine both TEM and SAXS.

**Acknowledgment** O. M. L., D. M., and M. K. acknowledge FAPESP, Brazil (2014/26672-8, 2011/01235-6 and 2011/02356-11), P. T., P. R., and L. M. S. Thanks to CONICET (Argentina). LNLS/CNPEM is acknowledged for SAXS measurements. LNNano/CNPEM is acknowledged for the use of TEM microscopes. All the authors want to especially thank the developers of the SASfit software, which was used to simulate the SAXS curves presented here.

## References

1. Feigin, L. A., & Svergun, D. I. (1989). *Structure analysis by small-angle X-ray and neutron scattering*. New York: Plenum Press.
2. Schnablegger, H., & Singh, Y. (2013). *The SAXS guide*. Austria: Anton Paar GmbH.
3. Li, T., Senesi, A. J., & Lee, B. (2016). Small angle A-ray scattering for nanoparticle research. *Chemical Reviews*, 116(18), 11128–11180.
4. Thiele, E. (1963). Equation of state for hard spheres. *The Journal of Chemical Physics*, 39(2), 474–479.
5. Glatter, O., & Kratky, O. (1982). *Small-angle X-ray scattering*. London: Academic.
6. Craievich, A. F. (2016). Small-angle X-ray scattering by nanostructured materials. In L. Klein, M. Aparicio, & A. Jitianu (Eds.), *Handbook of sol-gel science and technology*. Cham: Springer.
7. Debye, P., & Bueche, A. M. (1949). Scattering by an inhomogeneous solid. *Journal of Applied Physics*, 20, 51525.
8. Putnam, C. D., Hammel, M., Hura, G. L., & Tainer, J. A. (2007). X-ray solution scattering (SAXS) combined with crystallography and computation: Defining accurate macromolecular structures, conformations and assemblies in solution. *Quarterly Reviews of Biophysics*, 40(3), 191–285.
9. Hammouda, B. (2008). *Probing nanoscale structures – the SANS toolbox*. Maryland: Gaithersburg.
10. Glatter, O. (1977). A new method for the evaluation of small angle scattering data. *Journal of Applied Crystallography*, 10, 415–421.
11. Amemiya, Y., & Shinohara, Y. *Oral presentation at Cheiron School 2011: Small-angle X-ray scattering basics & applications*. Japan: Graduate School of Frontier Sciences, The University of Tokyo.
12. Sanjeeva Murthy, N. (2016). X-ray diffractions from polymers. In Q. Guo (Ed.), *Polymer morphology: Principles, characterization and processing* (pp. 29–31). Hoboken: Wiley.
13. Guinier, A., & Fournet, G. (1955). *Small-angle scattering of X-rays*. New York: Wiley.
14. Porod, G. (1982). Chapter 2: General theory. In O. Glatter & O. Kratky (Eds.), *Small-angle X-ray scattering*. London: Academic.

15. Roe, R.-J. (2000). *Methods of X-ray and neutron scattering in polymer science*. Oxford: Oxford University Press.
16. Hammouda, B. (2010). Analysis of the Beaucage model. *Journal of Applied Crystallography*, *43*, 1474–1478.
17. Rivas Rojas, P. C., Tancredi, P., Moscoso Londoño, O., Knobel, M., & Socolovsky, L. M. (2018). Tuning dipolar magnetic interactions by controlling individual silica coating of iron oxide nanoparticles. *Journal of Magnetism and Magnetic Materials*, *451*, 688–696.
18. Tancredi, P., Rivas Rojas, P. C., Moscoso-Londoño, O., Wolff, U., Neu, V., Damm, C., Rellinghaus, B., Knobel, M., & Socolovsky, L. M. (2017). Synthesis process, size and composition effects of spherical Fe<sub>3</sub>O<sub>4</sub> and FeO@Fe<sub>3</sub>O<sub>4</sub> core/shell nanoparticles. *New Journal of Chemistry*, *41*, 15033–15041.
19. Xu, R., Jiang, H., Song, C., Rodriguez, J. A., Huang, Z., Chen, C.-C., Nam, D., Park, J., et al. (2014). Single-shot three-dimensional structure determination of nanocrystals with femtosecond X-ray free-electron laser pulses. *Nature Communications*, *5*, 4061.
20. Barke, I., Hartmann, H., Rupp, D., Flückiger, L., Sauppe, M., Adolph, M., Schorb, S., Bostedt, C., et al. (2015). The 3D-architecture of individual free silver nanoparticles captured by X-ray scattering. *Nature Communications*, *6*, 6187.
21. Pedersen, J. (1994). Determination of size distribution from small-angle scattering data for systems with effective hard-sphere interactions. *Journal of Applied Crystallography*, *27*, 595–608.
22. Nakamura, K., Kawabata, T., & Mori, Y. (2003). Size distribution analysis of colloidal gold by small angle X-ray scattering and light absorbance. *Powder Technology*, *131*, 120–128.
23. Skou, S., Gillilan, R. E., & Ando, N. (2014). Synchrotron-based small-angle X-ray scattering of proteins in solution. *Nature Protocols*, *9*, 1727–1739.
24. Goertz, V., Dingenouts, N., Nirschl, H., et al. (2009). *Particle & Particle Systems Characterization*, *26*, 17–24.
25. Kohlbrecher, J. (2014). *SASfit: A program for fitting simple structural models to small angle scattering data*. Paul Scherrer Institute.
26. Pedersen, J. S. (1997). Analysis of small-angle data from colloids and polymer solutions: Modeling and least-squares fitting. *Advance in Colloid and Interface Science*, *70*, 171–210.
27. Khan, L. U., Muraca, D., Brito, H. F., Moscoso-Londono, O., Felinto, M. C. F. C., Pirota, K. R., Teotonio, E. E. S., & Malta, O. L. (2016). *Journal of Alloys and Compounds*, *686*, 453–466.
28. Orozco-Henao, J. M., Coral, D. F., Muraca, D., Moscoso-Londono, O., Mendoza Zelis, P., Fernandez van Raap, M. B., Sharma, S. K., Pirota, K. R., & Knobel, M. (2016). *The Journal of Physical Chemistry C*, *120*, 12796–12809.
29. Agbabiaka, A., Wiltfong, M., & Park, C. (2013). Small angle X-ray scattering technique for the particle size distribution of nonporous nanoparticles. *Journal of Nanoparticles*, *2013*, 640436.
30. Müller, J. J., Damaschun, G., & Hübner, G. (1979). Small angle X-ray scattering studies on the structure and symmetry of yeast pyruvate decarboxylase in solution. *Acta Biologica et Medica Germanica*, *38*(1), 1–10.
31. Pedersen, J. S., Oliveira, C. L. P., Hübschmann, H. B., Arleth, L., Manniche, S., Kirkby, N., & Nielsen, H. M. Structure of immune stimulating complex matrices and immune stimulating complexes in suspension determined by small-angle X-ray scattering. *Biophysical Journal*, *102*(10), 2372–2380.
32. Oliveira, C. L. P., Behrens, M. A., Pedersen, J. S., Erlacher, K., Otzen, D., & Pedersen, J. S. *Journal of Molecular Biology*, *387*(1), 147–161.
33. Moscoso-Londoño, O., Gonzalez, J. S., Muraca, D., Hoppe, C. E., Alvarez, V. A., López-Quintela, A., Socolovsky, L. M., & Pirota, K. R. (2013). *European Polymer Journal*, *49*(2), 279–289.
34. Moscoso-Londoño, O., Tancredi, P., Muraca, D., Mendoza Zélis, P., Coral, D., Fernández van Raap, M. B., Wolff, U., Neu, V., Damm, C., de Oliveira, C. L. P., Pirota, K. R., Knobel, M., & Socolovsky, L. M. (2017). Different approaches to analyze the dipolar interaction effects on diluted and concentrated granular superparamagnetic systems. *Journal of Magnetism and Magnetic Materials*, *428*, 105–118.

35. Meiorin, C., Moscoso-Londoño, O., Muraca, D., Socolovsky, L. M., Pirota, K. R., Aranguren, M. I., Knobel, M., & Mosiewicki, M. A. *Materials Chemistry and Physics*, 175, 81–91.
36. Baxter, R. J. (1968). Percus-Yevick equation for hard spheres with surface adhesion. *The Journal of Chemical Physics*, 49(6), 2770–2774.
37. Hansen, J. P., & Hayter, J. B. (1982). A rescaled mean spherical approximation structure factor for dilute charged colloidal dispersion. *Molecular Physics*, 46, 651–656.
38. Percus, J. K., & Yevick, G. J. (1958). Analysis of classical statistical mechanics by means of collective coordinates. *Physical Review*, 110(1), 1–13.
39. Rogers, F. J., & Young, D. A. (1984). New, thermodynamically consistent, integral equation for simple fluids. *Physical Review A*, 30, 999–1007.
40. Lee, L. L. (1995). An accurate integral equation theory for hard spheres: Role of the zero-separation theorems in the closure relation. *The Journal of Chemical Physics*, 103(21), 9388–9396.
41. Chen, S.-H., & Teixeira, J. (1986). Structure and fractal dimension of protein-detergent complexes. *Physical Review Letters*, 57, 2583.
42. Moscoso-Londono, O., Carriao, M. S., Cosio-Castaneda, C., Bilovol, V., Martinez Sanchez, R., Ledo, E. J., Socolovsky, L. M., & Martinez-Garcia, R. (2013). *Materials Research Bulletin*, 48, 3474–3478.
43. Schaefer, D. W. (1989). Polymers, fractals, and ceramic materials. *Science*, 243, 1023–1027.
44. Thesis. Physics Institute, University of La Plata. (2015).
45. Teixeira, J. (1988). Small-angle scattering by fractal systems. *Journal of Applied Crystallography*, 21, 781–785.
46. Moscoso-Londono, O., Muraca, D., Tancredi, P., Cosio-Castaneda, C., Pirota, K. R., & Socolovsky, L. M. (2014). Physicochemical studies of complex silver–magnetite nanoheterodimers with controlled morphology. *The Journal of Physics Chemistry C*, 118, 13168–13176.
47. Beaucage, G. (1995). Approximations leading to a unified exponential/power-law approach to small-angle scattering. *Journal of Applied Crystallography*, 28, 717–728.
48. Hernández, R., Sacristán, J., Nogales, A., Ezquerro, T. A., & Mijangos, C. (2009). Structural organization of iron oxide nanoparticles synthesized inside hybrid polymer gels derived from alginate studied with small-angle X-ray scattering. *Langmuir*, 25, 13212–13218.
49. Socolovsky, L. M., & Moscoso Londoño, O. (2017). Consequences of magnetic interaction phenomena in granular systems. In S. Sharma (Ed.), *Complex magnetic nanostructures*. Cham: Springer.
50. Chu, B., & Hsiao, B. S. (2001). Small-angle X-ray scattering of polymers. *Chemical Reviews*, 101(6), 1727–1762.
51. Ritland, H. N., Kaesberg, P., & Beeman, W. W. (1950). Double crystal and slit methods in small angle X-ray scattering. *Journal of Applied Physics*, 21(8), 838.
52. Bonse, U., & Hart, M. (1966). Small angle X-ray scattering by spherical particles of polystyrene and Polyvinyltoluene. *Zeitschrift Für Physikalische*, 189, 151–162.
53. Chu, B., Li, Y., Gao, T., Chua, B., & Ao, T. G. (1992). A Bonse–Hart ultrasmall angle x-ray scattering instrument employing synchrotron and conventional x-ray sources. *Review Scientific Instruments*, 63, 4128.
54. Amemiya, Y. (1997). X-Ray storage-phosphor imaging-plate detectors: High-sensitivity X-ray area detector, In: Academic Press (Ed.), *Methods enzymol.* 276th ed., Elsevier, (pp. 233–243).